GEOLOGY OF THE INTERMOUNTAIN WEST
an open-access journal of the Utah Geological Association
ISSN 2380-7601
Volume 11 *2024*

PIECING TOGETHER A PREHISTORIC PUZZLE: REGIONAL INFERENCES OF MICRO- AND MACROSCOPIC ANALYSES OF POSSIBLY ONE OF THE LAST HYBRID MAMMOTHS IN MAINLAND WESTERN NORTH AMERICA

Kate Morrison, Natalya Usachenko, Jonathan Erdman, Shilah Waters, and Renee L. Love

GEOLOGY OF THE INTERMOUNTAIN WEST

an open-access journal of the Utah Geological Association

ISSN 2380-7601

Volume 11 ***2024***

Production

Cover Design and Desktop Publishing
Douglas A. Sprinkel

Cover

Adolescent to young adult Jeffersonian Mammoth in Soda Springs, Idaho. Painted by University of Idaho undergraduate student Katie Ebling and used by permission. Inset photograph: Dr. Renee L. Love reconstructing the prehistoric puzzle of the mammoth crania that was fragmented during excavation in 1966 from southeastern Idaho.

Become a member of the UGA to help support the work of the Association and receive notices for monthly meetings, annual field conferences, and new publications. Annual membership is $30 and annual student membership is only $5. Visit the UGA website at www.utahgeology.org for information and membership application.

The UGA board is elected annually by a voting process through UGA members. However, the UGA is a volunteer-driven organization, and we welcome your voluntary service. If you would like to participate please contact the current president or committee member corresponding with the area in which you would like to volunteer.

Utah Geological Association formed in 1970 from a merger of the Utah Geological Society, founded in 1946, and the Intermountain Association of Geologists, founded in 1949. Affiliated with the American Association of Petroleum Geologists.

GEOLOGY OF THE INTERMOUNTAIN WEST
an open-access journal of the Utah Geological Association
Volume 11 ***2024***

Piecing Together a Prehistoric Puzzle—Regional Inferences of Micro- and Macroscopic Analyses of Possibly One of the Last Hybrid Mammoths in Mainland Western North America

Kate Morrison[1], Natalya Usachenko[2], Jonathan Erdman[3], Shilah Waters[4], and Renee L. Love[5]
[1]Department of Earth and Spatial Sciences, University of Idaho, Moscow, ID 83844-3022 USA; broo4823@vandals.uidaho.edu
[2] Department of Geosciences, Mississippi State University, Mississippi State, MS, 39762 USA; nu52@msstate.edu
[3]Department of Earth and Spatial Sciences, University of Idaho, Moscow, ID 83844-3022 USA; erdm4467@vandals.uidaho.edu
[4]Johns Hopkins Bloomberg School of Public Health, Baltimore, MD 21205, USA; sloosle1@jh.edu
[5]Department of Earth and Spatial Sciences, University of Idaho, Moscow, ID 83844-3022, USA; rlove@uidaho.edu

ABSTRACT

We evaluated the depositional age, taxonomy, diagenetic alteration, and osteology of mammoth skeletal remains from southeastern Idaho. In this study, we identified the first record of *M. jeffersonii* present in Idaho and only the second record of the species in Western North America that lived 13,586 to 13,444 cal BP. The mammoth remains were preserved in an ancient hot spring deposit and have indicators of possible pre-mortem injuries. The diagenetic processes post-mortem suggest that it was not immediately buried and was gnawed on by small and large carnivores. Our evaluation of the mammoth's tusks, molars, and limb bones suggest that these remains belonged to a young adult male that had been around 29 years old at its time of death. This specimen lived at a time when mammoths were becoming endangered in western North America before their ultimate disappearance from the fossil record.

INTRODUCTION

In the Late Pleistocene, 126 to 11.7 ka, *Mammuthus primigenius* (Woolly Mammoths) and *Mammuthus columbi* (Columbian Mammoths) had established populations in North America. Near the end of that epoch, between 14,690 to 12,890 Ka, Earth was experiencing the Bølling-Allerød Interstadial period, an abnormally warm period during the Ice Age that preceded the Younger Dryas (Broecker et al., 1988). It marks the retreat of the Laurentide and Cordilleran Ice Sheets and is a period where climate change played a major role in altering the North American biome. As the ice sheets melted, cold, dry conditions transitioned into a wetter, more temperate environment typical of modern conditions (Doerner and Carrara, 2001).

A north-south division of biomes allowed for multiple species of *Mammuthus* to cohabitate through niche partitioning (Yansa and Adams, 2012; Lister, 2017). For nearly 80 years, researchers (Osborn, 1942; Aguire, 1969; Saunders et al., 2010; Yansa and Adams, 2012; Enk et al., 2016; Widga et al., 2017) debated the validity of a third species: *Mammuthus jeffersonii* (Jeffersonian Mammoth). Recent genetic studies have suggested that the *M. jeffersonii* could either be a *M. primigenius, M. columbi* hybrid (Fisher, 2009; Enk et al., 2011), a subspecies of *M. columbi (*Aguire, 1969; Maglio, 1973; Graham, 1986; Lister, 2017*)*, or the product of introgression, which includes the hybridization and repeated backcrossing of genes between species through time (Enk et

Citation for this article.
Morrison, K., Usachenko N., Erdman, J., Waters, S., and Love, R.L., 2024, Piecing together a prehistoric puzzle—regional inferences of micro- and macroscopic analyses of possibly one of the last hybrid mammoths in mainland Western North America: Geology of the Intermountain West, v. 11, p. 21–44, Supplemental Material, https://doi.org/10.31711/giw.v11.pp21-44.

al., 2016). Genes of the extant African elephant (*Loxodonta africana*), close relative to both *Mammuthus* and *Elephas*, show introgressive behavior with recurrent backcrossing; this implies a genomic record response to ancient habitat changes (Roca et al., 2005).

Palynological records (Doernner and Carrara, 2001) indicate a transition from a colder, sedge brush-dominated landscape to a higher concentration of spruce and pine, and more temperate conditions similar to those of the modern day during the Bølling-Allerød period. This is coincident with sedge-grasslands disappearing into more closed forests in the Great Lakes region and *M. jeffersonii* competing with mastodon food sources (Yansa and Adams, 2012). The long history of introgressive radiation within mammoth populations through major fluctuations of interglacial and glacial periods, shows that they were not only interbreeding but also competing for food resources to survive (Yansa and Adams, 2012; Enk et al., 2016). Mammoth populations were declining, eventually leading to the megafaunal extinction event on the North American continental mainland (Bjorck et al., 1988; Agenbroad, 2005; Barnosky et al., 2015). Megafauna, including mammoths, disappeared from the rock record, and a total of 35 mammalian genera went extinct or became extremely endangered, with 90% of all mammals over 45 kg (99 lbs) disappearing from the continent (Gilmour et al., 2015). The primary driver of this extinction is still debated, although a combination of climate change and anthropogenic influences appears to be the most likely cause (Fisher, 2018).

A mammoth skeleton (specimen UISSM-001-COLA) was excavated from a hydrothermal spring deposit 11 km (7 mi) north of Soda Springs, Idaho, in 1966 and is now located at the University of Idaho (Jones and Bowers, 1968; Figure 1). This deposit was postulated to be Upper Pleistocene in age (Malde and Powers, 1962; Jones and Bowers, 1968) based on nearby geologic mapping and seven species of freshwater gastropods that were discovered between 61 to 91 cm (2–3 ft) above the mammoth remains. Original reconnaissance by R. Jones in 1968 mapped a tufa rim of an ancient discontinuous 'Pleistocene Spring' that was about 1.6 km (1 mi) in length. Nearly 100 springs have been mapped in the vicinity of Soda Springs and the Aspen Range to the east (Lewicki et al., 2013) and many have been associated with active and non-active accumulations of travertine deposits (Lewicki et al., 2013). The Pleistocene Spring is oriented against the east slope of a north-south-oriented fault block, along the trend with China Hat (Welhan et al., 2014; McCurry et al., 2015; Welhan and Breedlovestrout, 2016). The north-south-oriented fault block is part of the Paris thrust fault system within the Sevier fold and thrust belt in southeastern Idaho (Lewicki et al., 2013) and hydrothermal activity is associated with the Quaternary Blackfoot Volcanic Field (Welhan et al., 2014). Although more bones were searched for in the vicinity, the Pleistocene Spring was the only deposit to contain mammoth bones, which were discovered 2 m (6 ft) beneath the modern ground surface.

Here, we use several analytical techniques to evaluate taxonomy and paleontological history of UISSM-001-COLA. Specifically, the focus of this study was 5-fold: (1) precise radiometric dating of the molar, (2) pre- and post-mortem analysis of the health of the mammoth, (3) size, age, and gender determination, (4) diagenetic analyses, including recrystallization of bones and analysis of original material, and (5) taxonomic identification using the dimensions and morphology of the proboscidean's molars and mitochondrial DNA (mtDNA) analysis. This study provides a snapshot into the life of one of the last mammoths recorded in the fossil record on mainland Western North America during a time of great stress for Ice Age megabeasts, and provides unique insight into the impact of extinction drivers on Pleistocene megafaunal specimen. This megafauna specimen also records the presence of *Mammuthus jeffersonii* in the western United States, an area largely devoid of confirmed fossil evidence of the species.

MATERIALS AND METHODS

Radiometric Dating

Using a sterilized drill, material from the center of the molar was extracted and placed in a sterile plastic container. Samples were analyzed by Beta Analytic Testing Laboratory to obtain an Accelerator Mass Spectrometry (AMS) radiocarbon date. Pretreatment methods included washing the sample in hot hydrochloric

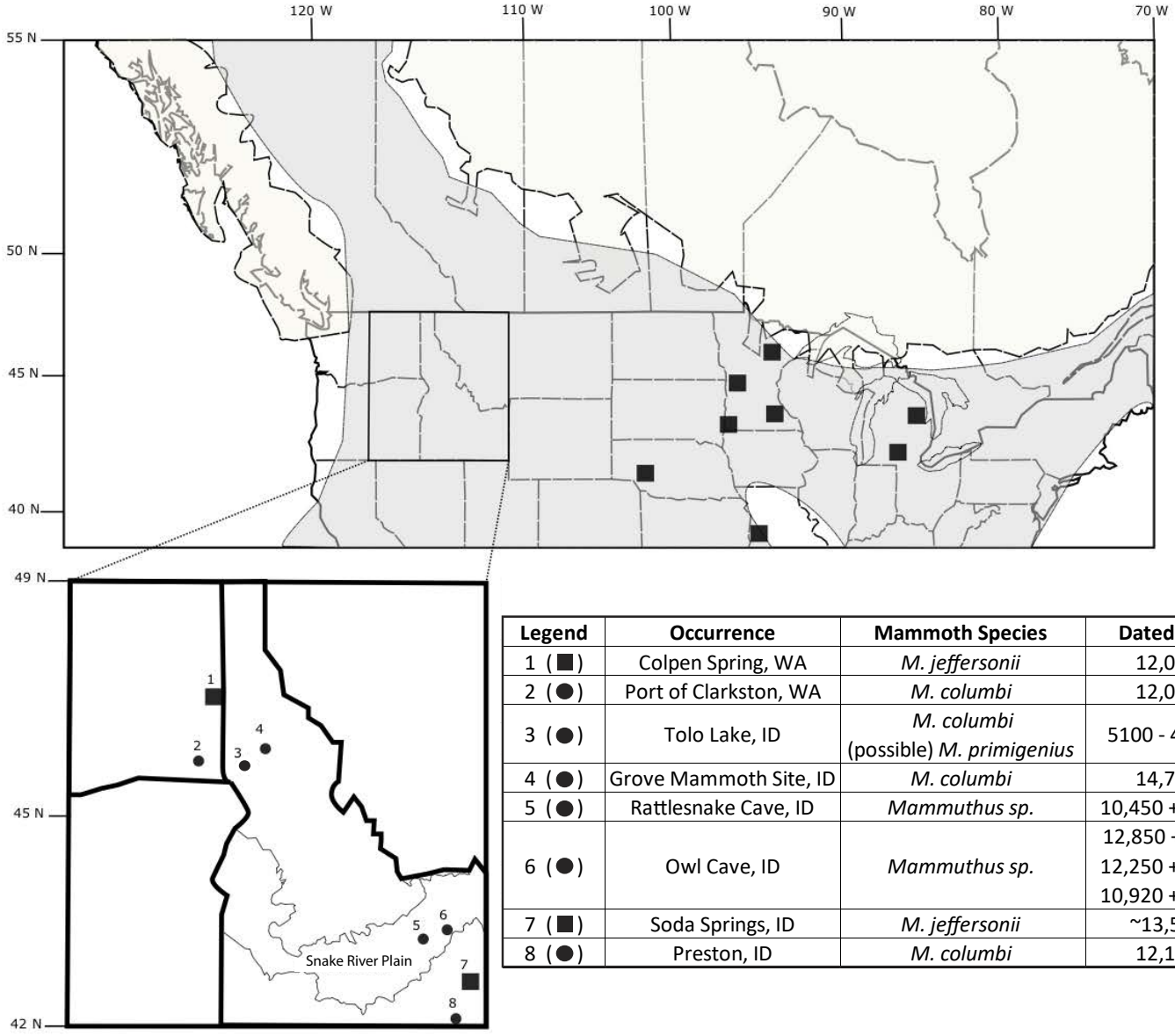

Legend	Occurrence	Mammoth Species	Dated Age
1 (■)	Colpen Spring, WA	*M. jeffersonii*	12,000
2 (●)	Port of Clarkston, WA	*M. columbi*	12,000
3 (●)	Tolo Lake, ID	*M. columbi* (possible) *M. primigenius*	5100 - 4300?
4 (●)	Grove Mammoth Site, ID	*M. columbi*	14,700
5 (●)	Rattlesnake Cave, ID	*Mammuthus sp.*	10,450 +/- 120
6 (●)	Owl Cave, ID	*Mammuthus sp.*	12,850 +/- 150 12,250 +/- 200 10,920 +/- 150
7 (■)	Soda Springs, ID	*M. jeffersonii*	~13,500
8 (●)	Preston, ID	*M. columbi*	12,150

Figure 1. Mammoth distribution in North America. Gray shaded area represents the inferred range of mammoths during terminal Pleistocene (15 to 10 Ka) based on Agenbroad (2005) and *Mammuthus* sp. in Faunmap (Graham and Lundelius, 2010). White shaded areas show extent of glaciation at this time. Mammoth discoveries attributed to *M. jeffersonii* are represented with a black square. Other mammoth species discovery sites are indicated with a black circle. Inset: Mammoth discoveries in Washington and Idaho that have been radiocarbon dated within 15 to 10 Ka. Descriptions of localities are included. Sites 1 through 3 sourced from Sappington (2019) and sites 4 through 8 are sourced from Agenbroad (2005).

acid (HCl) and alkali (NaOH) to remove carbonates and organic acids. Next the sample was bathed in sodium chlorite ($NaClO_2$) to eliminate wood cellulose that might be present. The techniques used to measure carbon-14 in the tooth utilized accelerator mass spectrometry. In calibrating the conventional radiocarbon date to calendar year equivalents, the High-Probability Density Range Method, INTCAL13, was used. The standard de-

viations are not reported less than ±30 BP to prevent from misrepresenting the accuracy of the results.

Pre- and Post-Mortem Analysis

External and internal features such as calluses, fractures, enlarged pores, distinct porosity, and ulcers identified on the mammoth skeleton can indicate a pre-mortem event or skeletal-related disease (Krzeminska and Wedzicha, 2015; Krzeminska et al., 2015; Leshchinskiy, 2017). A total of 271 bones and bone fragments were imaged at Gritman Medical Center in Moscow, Idaho, using computed tomography (CT) technology (see Supplemental Material for inventory of bones). The scans provided 18 DICOM files and full images of the limbs, axial skeleton, and manus bones of the mammoth. The images were analyzed using the processing software: Analyze 14.0 (AnalyzeDirect, Overland Park, KS), MicroDicom Viewer (MicroDicom Ltd, Sofia, Bulgaria), and ITK-SNAP (Yushkevich et al., 2006), and viewed in 3D Microsoft Paint to measure any abnormalities found internally such as enlarged pores and fractures and externally such as calluses and ulcers. The scans provided the ability to create 3D modeling of each bone for further assessment of surface features.

The bones of the mammoth were then organized into a categorized inventory and evaluated based on external features. To determine how much of the skeleton had been recovered, the specimen was divided into the following regions: limbs, vertebral column and ribcage, autopodial bones, crania, tusk, and pelvis (Supplemental Material). These features were recorded, along with a detailed description of preservation quality. Destructive features were documented and measured, and preservation quality was assessed using this scale: (1) very poorly preserved or severely fragmented, (2) poorly preserved or fragmented, (3) mostly preserved or slightly fragmented, and (4) well preserved or not fragmented (Table 1). The regions were then given a total percentage present value based on observational analysis and the preservation quality given. The total percentage of skeleton present was achieved from the average value of each region's total percentage intact combined.

Size, Age, and Gender Estimates

The ratios of metacarpal (MTC) III length vs. radius length and manus height vs. radius length of the skeleton were determined based on bone measurements and compared to those of different proboscidean species from Larramendi (2015) to show a comparison in body proportions. Manus height was calculated from Larramendi (2015) in which the length of the third metacarpal is multiplied by two. This is under the assumption that the length of the third metacarpal represents approximately 25% of the radius length in most proboscideans (Table 2). Using the following equation:

$$A = B \times C$$

where:

A = length of the specimen's frontal limb bone.

B = established percentage that the length of the respective limb bone is of the animal's total height.

C = total height from manus to shoulder, the height was estimated.

This height estimation was then compared to skeletal percentages for both *M. primigenius* and *M. columbi* (Larramendi, 2015; Table 3). To remain consistent with the calculations made for manus height in this study, the length of the radius was used to calculate the shoulder height of UISSM-001-COLA.

To determine the molar set that the mammoth was on at the time of death, we assessed the quantities of plates that were fully erupted and in wear, plates that were actively erupting and in wear, and plates that were in the process of erupting. These were compared to the data sets in Roth and Shoshani (1988) and Lee and others (2012), which estimated molar set number according to these parameters. Some authors (Lee et al., 2012; Lister, 2017; Widga et al., 2017) use the designation of m1-m3 for the premolars and M1-M3 for the adult molar sets. Here, we use the designation of M1-M6, which does not provide a distinction between the pre-molars and molars but lists all molars in order of eruption (Stansfield, 2015).

Table 1. Total percentage of specimen UISSM-001-COLA intact based on preservation quality.

Region	Total % Present	Preservation	Notes
Limbs	75	3	Left femur and ulna fragmented. Right femur not recovered.
Vertebral Column and Rib Cage	25	2	Many ribs and vertebrate with identified gnaw marks. Several missing components on the spinous process and rib cage.
Autopodial	95	4	Some phalanges missing.
Skull	20	2	Primarily fragments except for three, fully intact molars. Skull currently being reconstructed.
Tusks	90	1	Highly fragmented and fragile. Supported by plaster jacket.
Pelvis	5	1	Highly fragmented. Currently being reconstructed.
Entire Mammoth	51.70	2	Calculations based on the average percentage of each region.

Three methods were used to estimate UISSM-001-COLA's age at its time of death:

(1) Dentition – The approximate age of the mammoth was first estimated using dental analysis as outlined by Roth and Shoshani (1988). The length, width, height, and plate number of the specimen's right maxillary molar were measured to infer the respective molar set value and associated age range. In addition, states of eruption and wear were recorded on the four exposed mandibular molars. This method utilized the comparison of these measurements to fossil and extant *Elephas maximus* (Asian elephant) molars of known age, which are the sister taxon to *Mammuthus primigenius* (Roca et al., 2015; Enk et al., 2016), to provide an accurate analogy of elephantid maturation. These results were additionally compared to standards established in Laws (1966), as well as the records presented in Lee et al. (2012) and Haynes (2017), which assessed the molar characteristics of *Loxodonta africana* (African elephant).

(2) Post-Cranial Skeletal Assessment – Age parameters were further determined through the examination of the degree of epiphyseal fusion in the intact proximal and distal regions of UISSM-001-COLA's humerus, ulna, radius, tibia, and femur, which were categorized as fused, partially fused, or unfused (Lister, 1999; Haynes, 2017; Table 4). Postcranial bone growth increases in mammals until their epiphyses are fused to their diaphysis. African Elephant Equivalent Years (AEY; Lister,1999) are used to report relative mammoth ages. These were cross-referenced with the skeletal growth rates of modern proboscideans (Haynes, 2017), molar set number, and gender determination.

(3) Age Reference Line – The final method utilized reference points along the lower jaw to determine the Age Reference Point (ARP) and Age Reference Line (ARL) following the methods of Stansfield (2015; Figure 2). Using observed tooth lamellae along the endpoint of the ARL, an additional age estimation was made.

A hypothesis of the mammoth's gender was made predominantly using its tusk characteristics, which included girth and curvature (Averianov, 1996; El Adli et

Table 2. Ratios between metacarpal (MTC) III length vs. radius length and manus height vs. radius length of different proboscidean species found in Larraramendi (2015). Radius length from the proximal to distal end.

Species	Individual	MTC III length (mm)	Radius length (mm)	Calculated manus height (mm)	MTC III length vs. radius length (%)	Manus height vs. radius length (%)
Determined in this study	UISSM-001-COLA	210	889	420	23.6	47.2
Mammuthus primigenius	Pfannerhall	208	825	416	25.2	50.4
Mammuthus primigenius fraasi	Steinheim	245	955	490	25.7	51.3
Mammuthus trogontherii	Zhalainuoer III	255	985	500	25.9	51.3
Mammuthus meridionalis	Scoppito	266	950	525	28	51.8
Mammuthus meridionalis	Nogaisk	265	1040	530	25.5	55.3
Mammuthus columbi	MSL-140	237	948	474	25	51
Mammuthus columbi	NSM1597-62-2	194	823	388	23.6	50
Mammuthus columbi	SDSM 124688	244	928	488	26.3	47.2

Table 3. Height estimation of specimen UISSM-001-COLA based on limb bone measurements compared to specimens of Larramendi (2015).

Mammoth Species	Larramendi (2015) Percentages	UI-SSM-001COLA Radius Length (cm)	Total Height of UISSM-001 COLA (cm)
M. primigenius	26.67	88.9	333.33
M. columbi	27.10	88.9	328.04

al., 2015), and the degree of epiphyseal fusion observed in the radius, ulna, humerus, tibia, and femur (Lister, 1999; Stanfield, 2015; Haynes, 2017; Figure 3 and Table 4). Although an assessment of the pelvis would be ideal for more accurate gender determination, UISSM-001-COLA's pelvis was severely fragmented upon excavation and could not be analyzed. Instead, since mammoths were sexually dimorphic in body size and differed in their rates of skeletal maturation, we were able to use the size, shape, and length of their tusks to determine gender (Laws, 1966; Averionov, 1996; Haynes, 2017). The appearance of the mandibular condyles was also considered; in males, these structures are more circular, whereas in females they are more ovular (Yacobi et

Table 4. Specimen UISSM-001-COLA's limb bones with degree of epiphyseal fusion. Findings are compared to Lister (1999) and suggest an age range of around 29 AEY.

Bone	Epiphyseal fusion	Dental age (AEY) from Lister (1999)	Haynes (2017) corrected age using Stansfield (2015)
Distal humerus	Fused	≥6	≤24
Proximal tibia	Fused	≥26	27-30
Distal tibia	Fused	≥26	≤24
Proximal ulna	Fused	≤34	≤24
Distal femur	Fused	≤34	29-33
Proximal humerus	Unfused	≤41	40-47
Proximal femur	Unfused	≤43	37-42
Distal radius	Unfused	≤43	
Distal ulna	Unfused	≤43	≥52

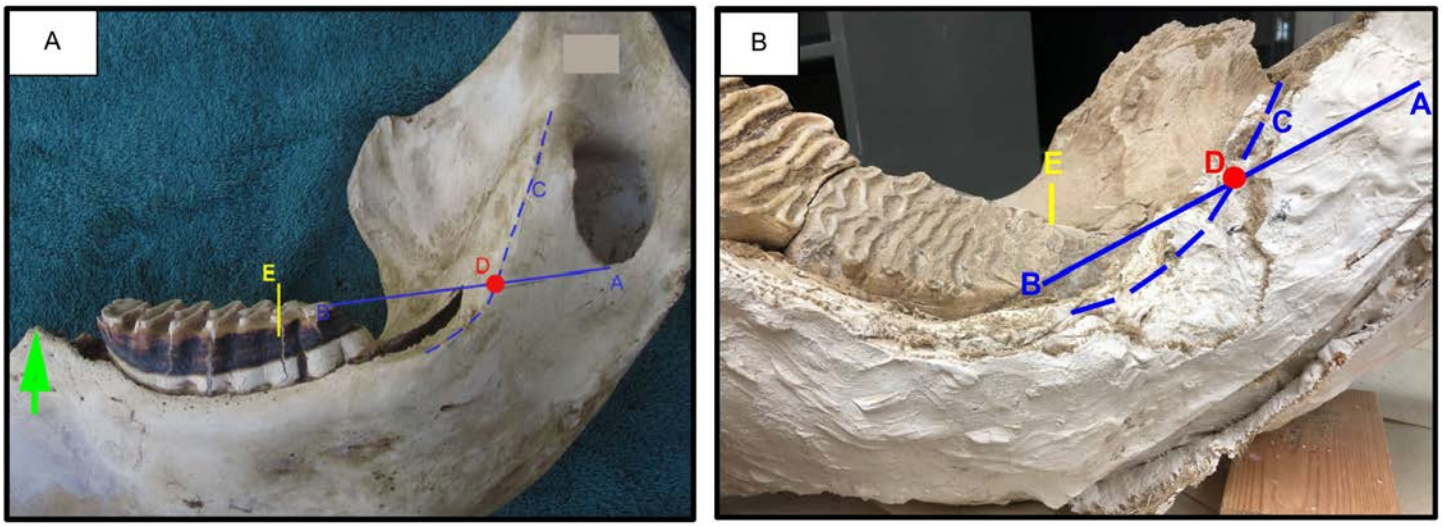

Figure 2. Age estimation using the ARL (Stansfield, 2015). (A) A straight line was drawn from point A (the base of the mandibular foramen) to point B (the most distal section of molar occlusal wear). A second line, C, was visualized along the ridge of the medial mandible, and intersects the first line at point D, which is known as the ARP. From this point, a distance of 10 cm (3.94 in) was measured, passing centrally, through the distal molar. This is the ARL. The yellow line E marks the endpoint of the 10-cm (3.94 in) measurement in this example from Stansfield (2015). (B) Age Reference Line calculation on specimen UISSM-001-COLA.

al., 2004). The last indirect method used to determine gender was to assess the epiphyseal regions in the limb bones; in females, the epiphyses would typically finish fusing between ages 30 and 35, and in males, between 45 and 50 (Lister, 1999; Haynes, 2017).

Diagenetic Analysis

The fossilization of bone is characterized by the replacement of protein and other organic biomolecules with inorganic material and the recrystallization of inorganic remains, such as hydroxyapatite in bone, into

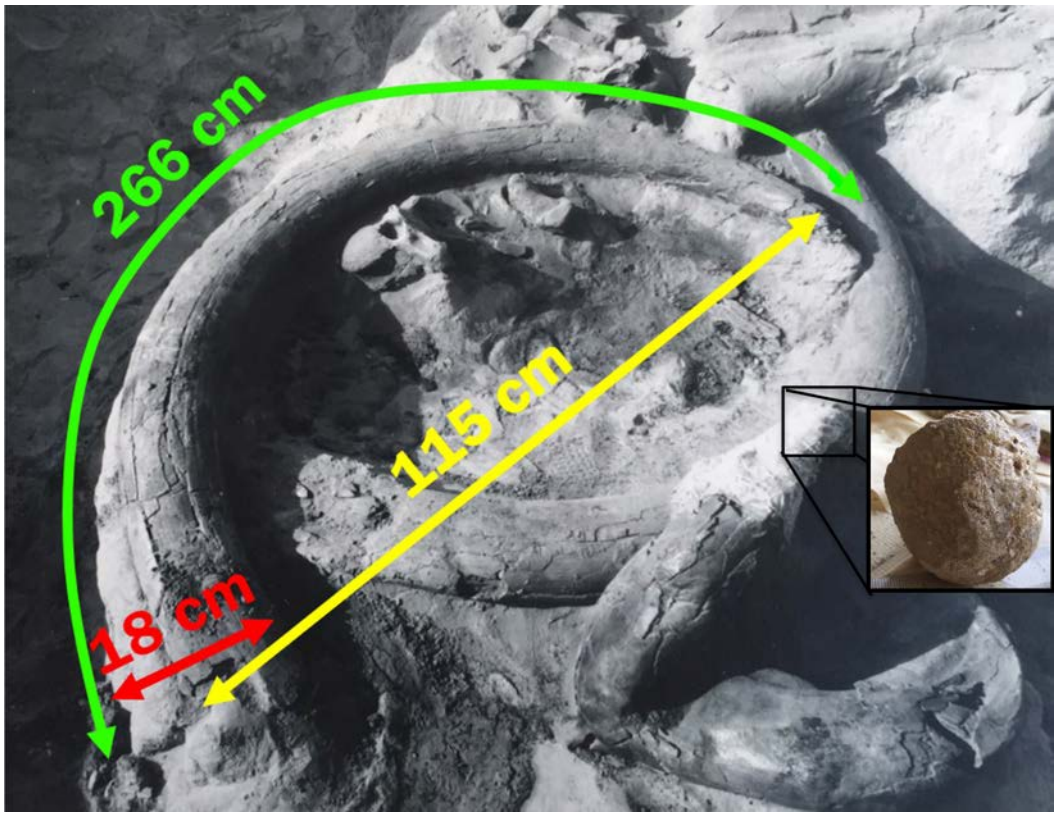

Figure 3. Curvature of tusks, length, and girth. Green arrow showing curved length of 266 cm (105 in). Yellow arrow showing a non-curved length of 115 cm (45 in). Red arrow showing width of distal end at 18 cm (7.1 in). Inset image showing the circularity of mandibular condyle.

a more stable form (Pfretzschner, 2004; Buckley and Wadsworth, 2014; Keenan et al., 2015; Kendall et al., 2018). Environments most suitable to preservation are those that are unfavorable to microbial activity; remains most likely to avoid diagenesis are those consisting of or encased by hydrophobic, inorganic lattices that are impermeable to water and are, therefore, protectant against biotic and abiotic decay (Hedges et al., 1995; Trueman and Martill, 2002; Jans, 2008; Keenan, 2016). Therefore, some hard surface remains, such as bone and teeth that have inorganic casings, can protect biomolecules including nucleic acids, proteins, lipids, and carbohydrates from degradation. This can, in turn, enable certain chemical and molecular analyses, which could provide insights into genetic information and environmental conditions.

To determine the diagenesis of the bones, and to assess whether original material was remaining in the bones for genetic analysis, the external surface structure of a tusk and tooth were imaged using scanning electron microscopy (SEM). Superficial samples were collected from the tusk and tooth for analysis. The samples were prepared with a carbon coating to gain high resolution and imaging under the SEM. Elemental composition of each specimen was determined utilizing SEM with energy dispersive spectroscopy (SEM/EDS). This analysis was performed on both external surface samples and internal samples. Internal samples were obtained by drilling into the tusk, tooth, and femur. Two samples were collected from the interior tusk, three from the tooth (outer, middle, inside), and two from the femur (epiphysis and diaphysis). Samples were then imaged without a carbon coat to obtain accurate elemental composition profiles from EDS. The molecular composition of the tusk was acquired using x-ray diffraction (XRD) performed at 40 kV. A total of 1561 data points were generated over a spectrum of 0 to 80°. Steps equaled 0.05° in measurements of two-theta.

Taxonomic Identification

Proteinaceous composition of UISSM-001-COLA was determined using methods of Cappellini et al. (2018) to determine if original material was remaining in the specimen for radiocarbon dating and taxonomic analysis. A femoral sample was collected using a sterilized drill at the junction between the articular surface of the knee and the shaft, just proximal to the epicondyle, at a depth of approximately 1 cm (0.4 in). When drilling into the bone, the periosteum was discarded to minimize contamination. Treatment buffer was prepared using 0.125 M Tris-Cl, 4% SDS, 20% v/v glycerol, 0.2 M DTT, and 0.02% bromophenol blue with a pH of 6.8. A sample of 15 mg was boiled for 15 minutes and then the sample was loaded into an SDS gel composed of a 10% resolving gel and a stacking gel. Polyacrylamide gel electrophoresis (PAGE) was run for approximately 30 minutes to allow separation of the proteins and other components of the femur. The gel was stained with Coomassie brilliant blue R-250 solution.

Taxonomic identification of UISSM-001-COLA was determined in two ways: (1) by using measurements of molar characteristics adapted from Maglio (1973) and Lister (2017), and (2) by extracting mtDNA from a tooth sample. Measurements of UISSM-001-COLA's molar included length (L), width (W), height of crown (H), enamel plate count (P), lamellar frequency (LF), and hypsodonty index (HI). The LF was calculated on an average of six measurements taken from the upper, middle, and lower portion of the crown on both the lingual and buccal side. The HI was calculated as HI = H/W x 100, or height of the crown as an expression of width standardized to a length of 100 mm (3.9 in). These measurements were obtained using a digital caliper on the maxillary right molar (Figure 4). No estimation of missing plates was required due to the presence of the anterior-most root. The molar parameters of the specimen were then compared between holotypes or neotypes of *M. primigenius*, *M. columbi,* and *M. jeffersoni* (Roth and Shoshani, 1988; Lee et al., 2012; Lister and Sher, 2015; Haynes, 2017; Lister 2017; Widga et al., 2017; Table 5).

Elemental composition analysis provided guidance on where to sample for mtDNA. The anterior talon of the upper molar was sent to the University of California, Santa Cruz Paleogenomics Lab, for analysis. Extraction and processing were performed according to Dabney et al. (2013). Initial sample preservation and assessment was performed using a single-stranded library preparation and sequencing on an Illumina NextSeq 2x150 run targeting 1 million raw reads. The reads were trimmed and aligned to *Loxodonta africana* nuclear genome and *Mammuthus primigenius* mitochondrial genome. Subsequently, the sample underwent mtDNA preparation and analysis using methods according to Kirillova et al. (2017), myBaits v4.01 protocol (Biodiscovery, LLC dba Arbor Biosciences, 2018), and Vershinina et al. (2020). Sequencing occurred on an Illumina NextSeq 2 x 150 run targeting 0.5 million raw reads. Afterwards, the reads were trimmed, merged, and filtered using Seqprep2 (https://github.com/jstjohn/SeqPrep), FASTX_ToolKit (http://hannonlab.cshl.edu/fastx_toolkit/), and PRINSEQ lite (Schmieder and Edwards, 2011). The final consensus sequence was generated using MIA (https://github.com/mpieva/mapping-iterative-assembler) and compared to clades described in Enk et al. (2016) to assign UISSM-001-COLA to a haplogroup.

RESULTS

Radiometric Dating

Radiocarbon dating was consistent with the estimated upper Pleistocene age derived from the gastropod identification and yielded a age of 13,586 to 13,444 cal BP with 95.4% probability (Figure 5; Beta Analytic Testing Laboratory specimen number: 524280). A C:N ratio was also obtained to test potential diagenetic alteration or contamination at 3.2, with an isotope ratio mass spectrometer reading of δ13C at –18.7 ‰ and δ15N at +11.32 ‰. Modern bone is in the range of 2.9 to 3.5, suggesting that little to no diagenetic alteration or contamination occurred (DeNiro, 1985; Enk et al., 2016).

Pre- and Post-Mortem Analysis

A total of 271 bones and bone fragments were itemized (Supplemental Material). The pelvis and crania have significant damage and are currently in fragments.

Table 5. Total averages and ranges of dental parameters from Widga et al. (2017) and Lister (2017) with comparison to those of specimen UISSM-001-COLA. Note: specimen UISSM-001-COLA's measurements of the upper right M5 molar better coincides with *M. columbi* for the plate number and enamel thickness, and *M. primigenius* for the lamellar frequency and width. The length, height, and hysodonty index are similar for each of the species. All measurements in mm.

Taxonomic ID	Molar Position	Plate Number		Length		Height		Width		Enamel Thickness		Lamellar Frequency		Hypsodonty Index	
		Average	Range	Average	Range	Average	Range	Average	Range	Average	Range	Average	Range	Average	Range
M. columbi	M3(M6) Right Side	18.9	18-21	268.6	180-359	181.1	161-216	101.3	69-106	3.1	2.0-3.0	5.6	5.29-7.53	209.1	176.7-253.25
	M3(M6) Left Side	18	15-19	268.2	166-315	179.2	112-220	91.6	69-108	2.9	2.0-3.0	6	5.71-7.12	207	162.32-243.68
	M3(M6) Side Unspecified	19.1	18-24	276.3	260-340	194.5	152-290	103.8	74-128	2.4	1.6-3.9	6.1	5.88-7.69	191.4	158.44-246
	Total	18.9	15-24	272.6	166-359	190.1	112-290	102.2	69-128	2.6	1.6-3.9	6	5.29-7.69	196.1	158.44-253.25
	M2(M5) Side Unspecified	10.2	4.0-16.0	119.2	138-199	147	131-162	88.1	68-111.4	2.2	1.5-2.5	6.4	4-8.71	115	0-217.65
M. primigenius	M3(M6) Right Side	24.6	20-28	272.6	205-328	173.4	102.1-219	93.5	72-122	1.8	1.03-2.83	8.5	6.91-10.94	189.4	128.27-230.77
	M3(M6) Left Side	24.7	20-28	267.4	195-325	148.8	102.2-179	96.5	80.9-116	1.8	1.3-2.37	8.3	7.23-10.16	158.8	103.44-187.64
	M3(M6) Side Unspecified	23.8	21-30	271.8	260-355	172.6	155-213	94.9	75-125	1.5	1-2.1	8.3	6.15-10	157.6	168-227.6
	Total	24.2	20-30	271	195-355	167.4	102.1-219	94.9	72-125	1.6	1-2.83	8.4	6.15-10.94	167.4	103.44-230.77
	M2(M5) Side Unspecified	13.4	9.0-16.0	166.6	77-214	131.6	92-162.9	71.2	50-89	1.6	1.5-1.825	8.8	6.54-11.76	113.8	0-201.73
M. jeffersonii	M3(M6) Right Side	22.4	19-31	287.4	214-380	178	134.4-249	101.9	88-120	2.2	1.5-2.9	7.5	5-10.19	173.5	74.26-235.96
	M3(M6) Left Side	23.4	22-27	282	250-305	153.4	75-210	94.9	80.7-108.5	2.5	1.5-2.1	6.6	7.2-8.07	184.7	133.98-218.56
	M3(M6) Side Unspecified	27	27	295	295	206	202-210	110.6	103-117	2	1.3-2.7	8.8	8.8	188.3	172.65-203.88
	Total	23	19-31	285.8	214-380	173.4	75-210	101.6	80.7-120	2.3	1.3-2.9	7.3	5-10.19	178	74.26-235.96
	M2(M5) Side Unspecified	15		241				83		1.8		6.2		0	
UISSM-001-COLA	M2(M5) Upper Right		19		278		154		82.8		2.4		8		186

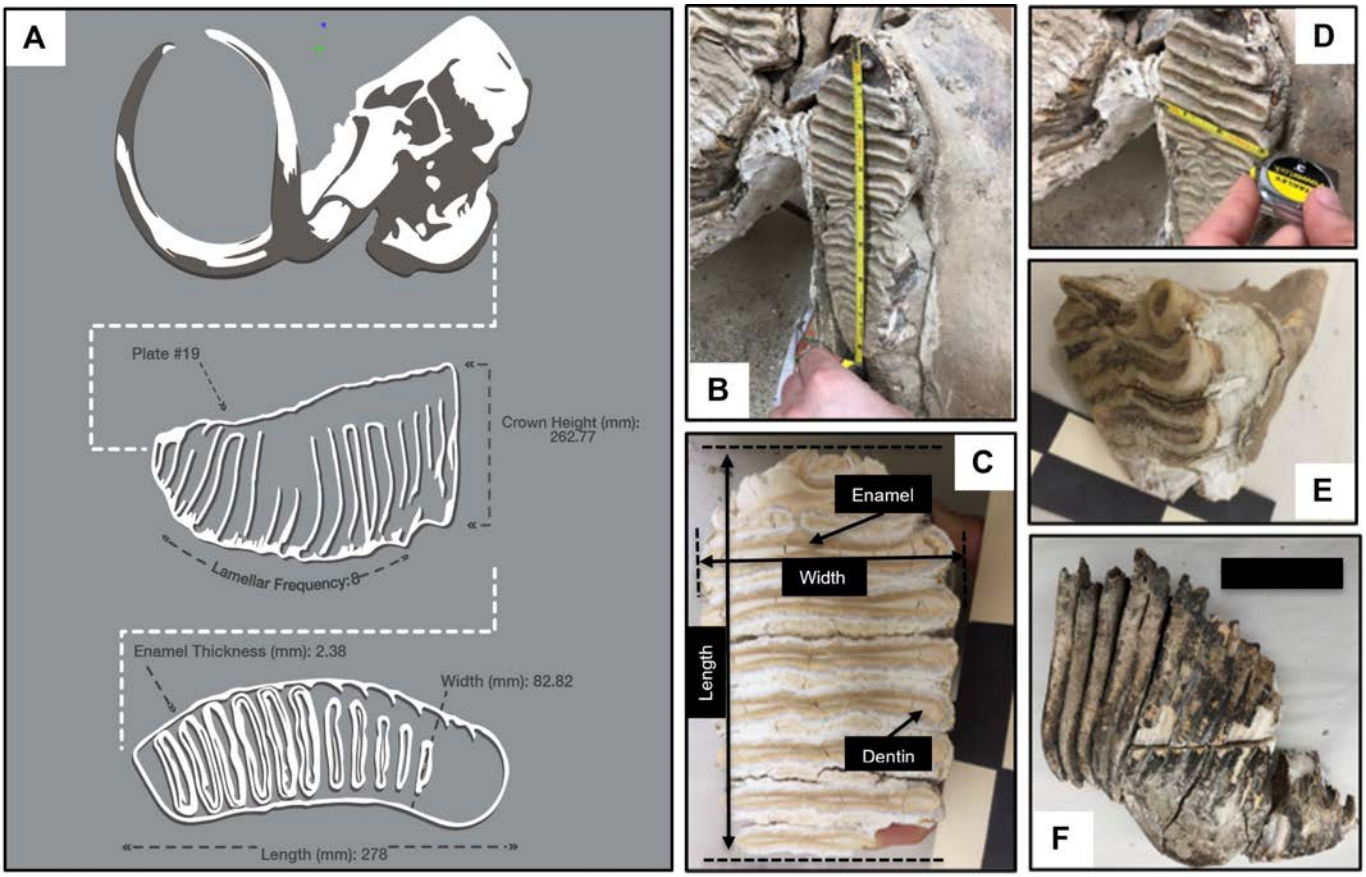

Figure 4. Analysis of molars. (A through D) Assessment of molar parameters. (B through D) Characteristics of mammoth molars showing plate, lamellar frequency, and enamel thickness. Modified from Roth and Shoshani (1988). (E through F) Upper teeth.

The tusks have also experienced a large amount of fracturing. The limb bones have significant breaks that separate them into two to three fragments. The right humerus is missing except for the proximal epiphysis. The vertebral column only shows small amounts of fracturing, but the ribs have significant damage, and most are missing. An estimated 10% of the mammoth's ribcage is present. Due to the large amount of fragmentation of the ribs, a full reconstruction was not possible. The manus and pes bones are well-preserved and exhibit only small amounts of fragmentation. Observational analysis of the preservation quality showed that UISSM-001-COLA has an overall average quality number of 2 out of a scale of 4. The total percentage of UISSM-001-COLA's intact skeleton was estimated to be 51.7% (Table 1). Whereas over half of the remains were present for analysis, larger portions of the vertebral column, ribcage, crania, and pelvis were unrecovered or in fragments.

External and internal observations revealed unusual markings and features on the joints, limbs, and autopodial bones, and can be indicators of premortem health conditions and injuries. The ribs of the mammoth contain gnaw markings with sizes ranging from presumed small mammalians to large carnivores. The marks on the ribs are currently under more investigation and will not be discussed further in this paper. An internal fracture, approximately 5.05 cm (2 in) in length, occurs inside the right calcaneum bone and is identified by a thickened callus around the fracture. The left calcaneum bone of the mammoth showed enlarged pore sizes of up to 3 mm (0.12 in) in diameter; this is in contrast to normal ranges for pores that are typically less than 0.1 mm (Leshchinskiy, 2012). Premortem deformations by ulcers were identified by an area up to 6 cm^2 (2.4 in^2) with a linear dimension typically no larger than 7 cm (2.8 in). These features are common on

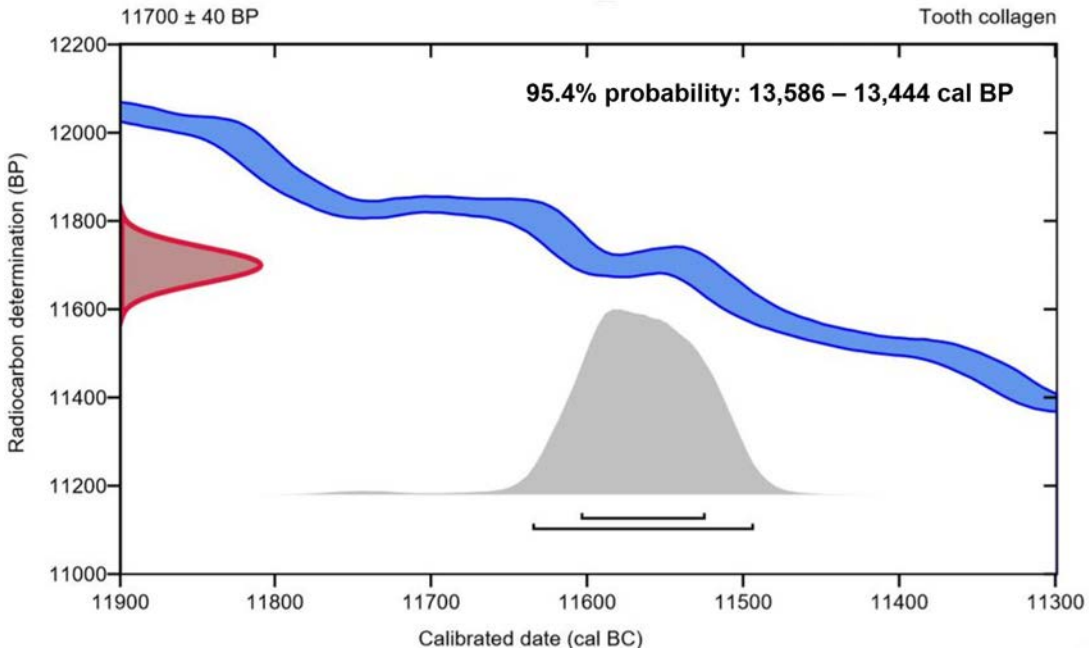

Figure 5 . Conventional radiocarbon age for specimen UISSM-001-COLA is 13,586 to 13,444 cal BP. Date provided by Beta Analytics Laboratory.

the articular surface. This mammoth presents a feature that matches this description on the distal end of its humerus measuring 4 x 4.5 cm (1.6 x 1.8 in). These ulcers were compared to Leshchinskiy (2017) to confirm the identification. The seventh thoracic vertebra presents an oval-shaped deformation measuring 2 x 1.5 cm (0.8 x 0.6 in) which may be a premortem ulcer or a result of peripheral erosion on the articular surface.

Specimen UISSM-001-COLA shows significant dilation in the Haversian cavities of the axis. Studies have found that non-osteoporotic indications within Haversian bones of these large animals would measure at typically less than 0.1 mm (Leshchinskiy, 2012). The vertebral column of mammoths can indicate external signs of osteological changes with distinct porosity represented as numerous small, piercing holes (Krzeminska and Wojtal, 2015; Leshchinskiy, 2017). This feature is present in UISSM-001-COLA's seventh thoracic vertebra. These features are shown in Figures 6 and 7.

Size, Age, and Gender Estimates

Specimen UISSM-001-COLA's jaw had a base alveoli diameter of 18.9 cm (7.4 in) and was fairly circular, indicating the specimen may have been a male. Female alveolar diameters typically range between 8 and 10 cm (3 and 3.9 in) (Pilgrim and Western, 1983; Vereschchagin and Tikhonov, 1986; Averianov, 1996; Moss 1996). The length and curvature of the specimen's tusk (Figure 3) suggest that UISSM-001-COLA was a sexually mature male. Female tusks tend to be slenderer, straighter, and more cylindrical in shape (Fisher, 2009), and whereas male tusks are generally more massive, more conical in shape, and turned medially at the adult stage (Lister and Bahn, 2007). Based on the specimen's tusk characteristics, alveoli diameter, and the degrees of epiphyseal fusion in the limb bones (Figures 8 and 9; Table 4), it can be concluded that UISSM-001-COLA was a male mammoth.

A morphological comparison of UISSM-001-COLA's molars to those presented in Roth and Shoshani (1988) determined that UISSM-001-COLA would have already aged out of its first three sets of deciduous molars. One of its adult molar sets was in wear at its time of death. Based off the dental aging standards of living elephants, mammoths would wear through and then lose each set of molars at approximately age 1, 5, 10, 22,

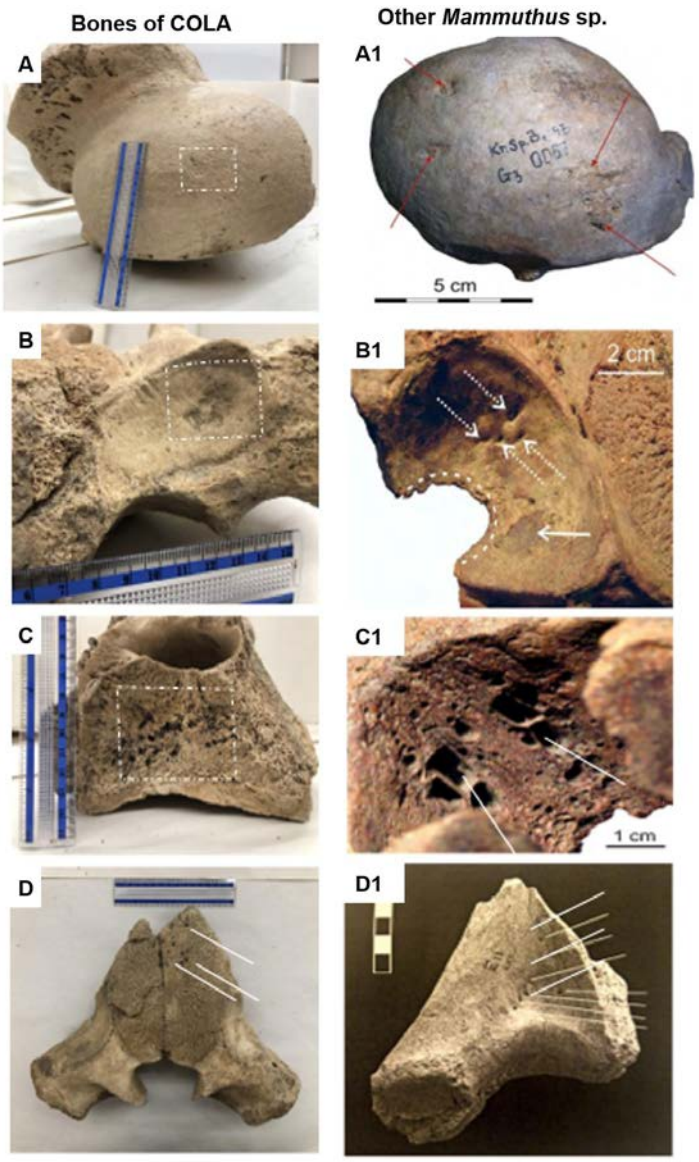

Figure 6. (A) Premortem deformation by ulcer on the distal end of the humerus bone measuring 4 x 4.5 cm (1.6 x 1.8 in) outlined in white, dashed box. (A1) Premortem deformations by ulcers indicated by red arrows from Leshchinskiy (2012) for comparison. (B) Premortem ulcer or a result of peripheral erosion on the articular surface outlined in white, dashed box. (B1) Premortem deformations by ulcers indicated by white arrows from Leshchinskiy (2017) for comparison. (C) Dilation of cavities opening into the vertebra foramen indicated by dashed, white box. (C1) Diliation of cavities opening into the vertebra foramen from Leshchinskiy (2017) for comparison. (D) Distinct porosity in the seventh thoracic vertebra indicated by white arrows. (D1) Distinct porosity shown with white arrows from Krzeminska et al. (2015) for comparison.

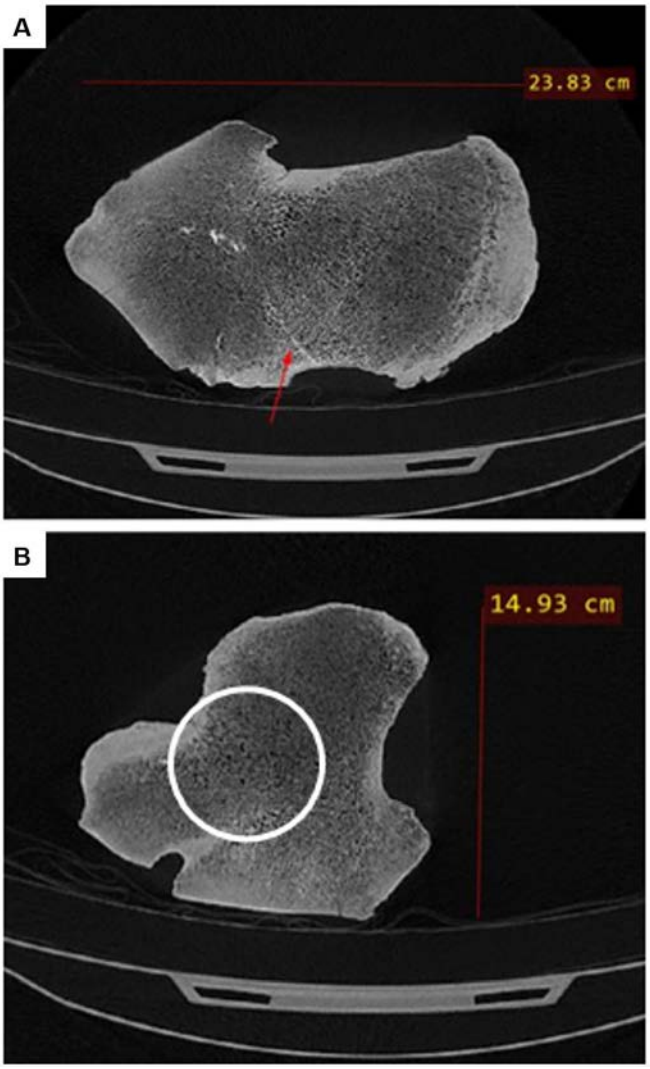

Figure 7. CT rendering of the mammoth's right (A) and left (B) calcaneum bones. Potential fracture indicated by red arrow. Enlarged pores indicated by white circle.

35, and 65 (M1, M2, M3, M4, M5, and M6, respectively; Laws 1966; Lee et al., 2012). A comparison of measurements between UISSM-001-COLA's molars and the values listed in Roth and Shoshani (1988) and Lister (2017) suggest that the specimen's 4th set of molars (M4 molars) had fully erupted, were in wear, and were almost completely gone, and its 5th molar set (M5) was almost fully erupted and in wear, placing its approximate age between 22 and 35, respectively (Table 5; Figure 4). The Age Reference Line endpoint fell between the 10th and 11th lamella of the mammoth's left mandibular mo-

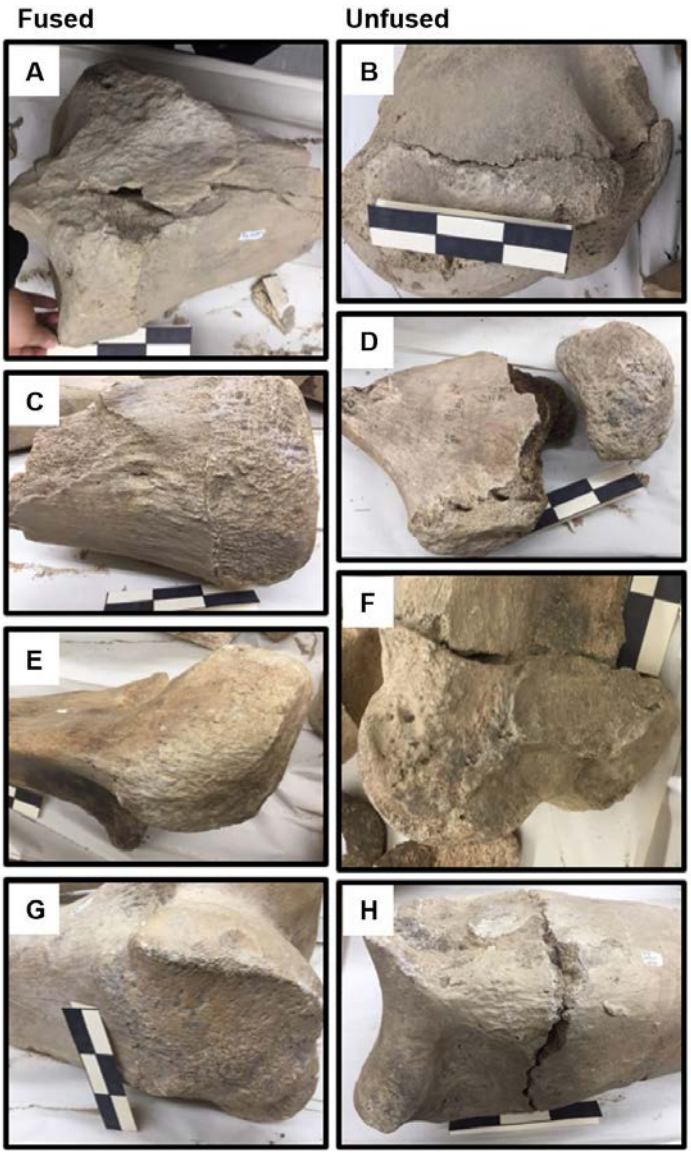

Figure 8. Assessment of the epiphyseal fusion in limb bone fragments with scale. (A) Proximal tibia; fused. (B) Proximal humerus; unfused. (C) Distal tibia; fused. (D) Proximal femur; unfused. (E) Proximal ulna; fused. (F) Distal radius; unfused. (G) Distal femur; fused. (H) Distal ulna; unfused.

lar (Figure 2). Since this molar is an M5, the estimated age would be 28 to 29 AEY (using Lee et al., 2012, age class; Stansfield, 2015). Analysis of the mammoth's front and rear limb bones revealed that none of the later epiphyseal plates had yet fully fused at its time of death, which places the estimated age range between 29 and 33 AEY (Figure 8) according to the classifications of Lister (1999) and Haynes (2017). Using the categories established by Lee et al. (2012), the specimen would lie somewhere between 27 and 31.5 years old. Stansfield's (2015) age reference line corroborates these age ranges with an estimate of 28 to 29 years old (Figure 9). Therefore, the ontogenetic age of the specimen was postulated to be 29 AEY, as this was the age in common between all these estimates.

Diagenetic Analysis

The SEM images revealed that the tusk exhibits high levels of porosity and permeability. The tooth, conversely, appears striated but generally remains predominantly non-porous (Figure 10). The EDS spectra demonstrated that most of the tusk, tooth, and femur are composed of calcium, phosphorus, and oxygen (Figure 11). Carbon is also present, but to a much smaller extent. Considering the quality of the remains as well as the length of time since excavation, the major compound composing these samples is apatite – $Ca_{10}(PO_4)_6(OH)_2$. The EDS spectra further suggested some elemental replacement in the apatite, as illustrated by the presence of fluorine. These conjectures are confirmed according to the XRD performed on the tusk (Figure 12).

Whereas the majority of the tusk, tooth, and femur samples contain only minimal amounts of carbon relative to other elements, a high proportion of carbon occurs in some fragments of the interior tooth sample. However, the amount of carbon in the interior tooth sample is not homogenous; generally, the smaller fragments have higher fractions of carbon (Figure 11). The SEM revealed additional crystalline structures on the surface of the tusk and potential surface contaminants. EDS inspection of the crystalline structures demonstrates predominant components of calcium, phosphorus, carbon, and oxygen. The main suspected surface contaminants appear fibrous and, according to EDS, have high levels of carbon. No protein occurred in the mammoth femur after processing and running PAGE.

Taxonomic Identification

The ratios found between the metacarpal (MTC) III length vs. radius length and manus height vs. radius length in UISSM-001-COLA were found to be small-

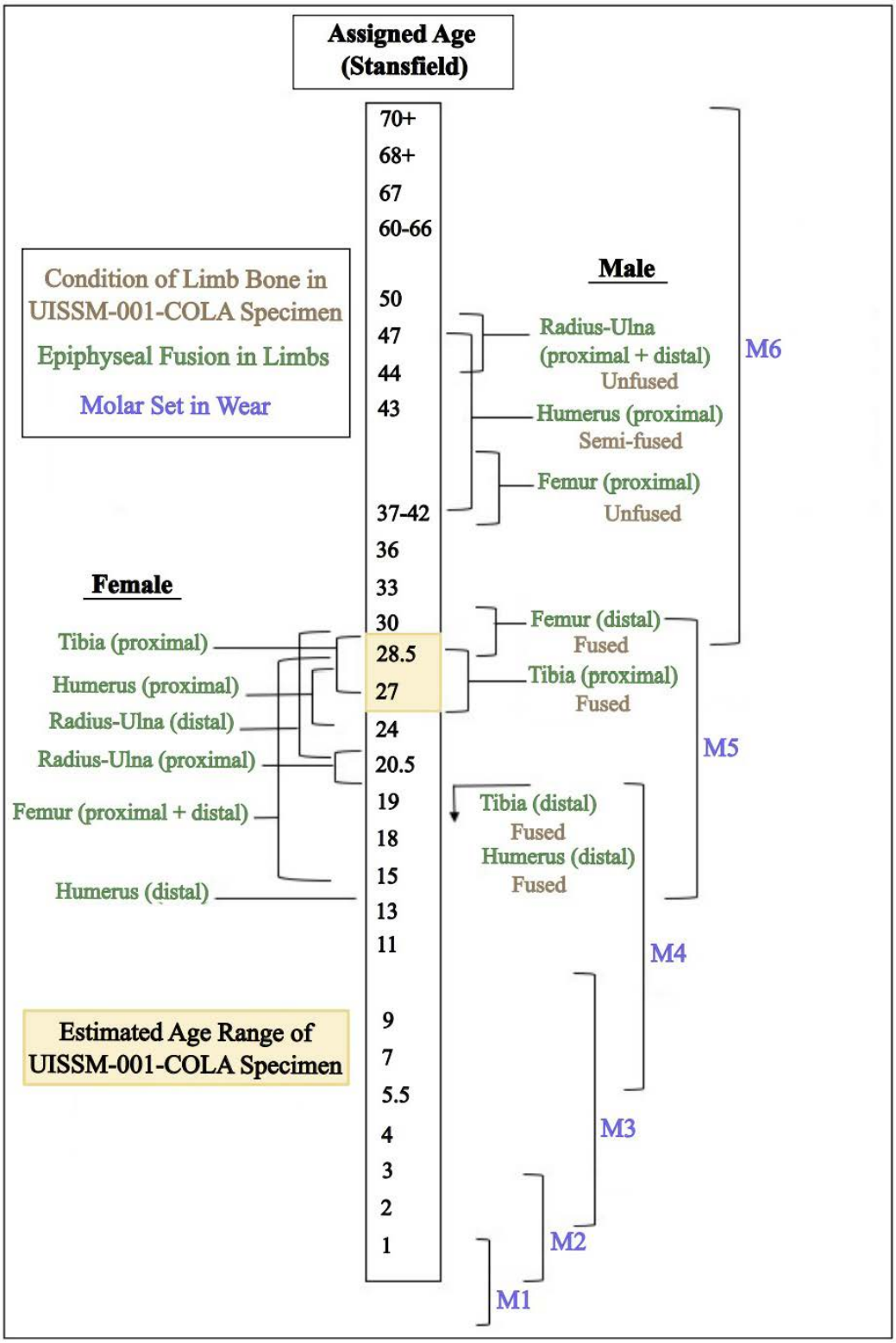

Figure 9. Age estimation for specimen UISSM-001-COLA based on a correlation of the condition of its epiphyses (see Table 4) with prior correlations between molar wear and epiphyseal fusion in male and female specimens of *Loxodonta africana*. Modified from Haynes (2017). Overlap of the age estimate with the 5th set (M5) and degree of the epiphyseal fusion discounts that we could have only the 4th molar.

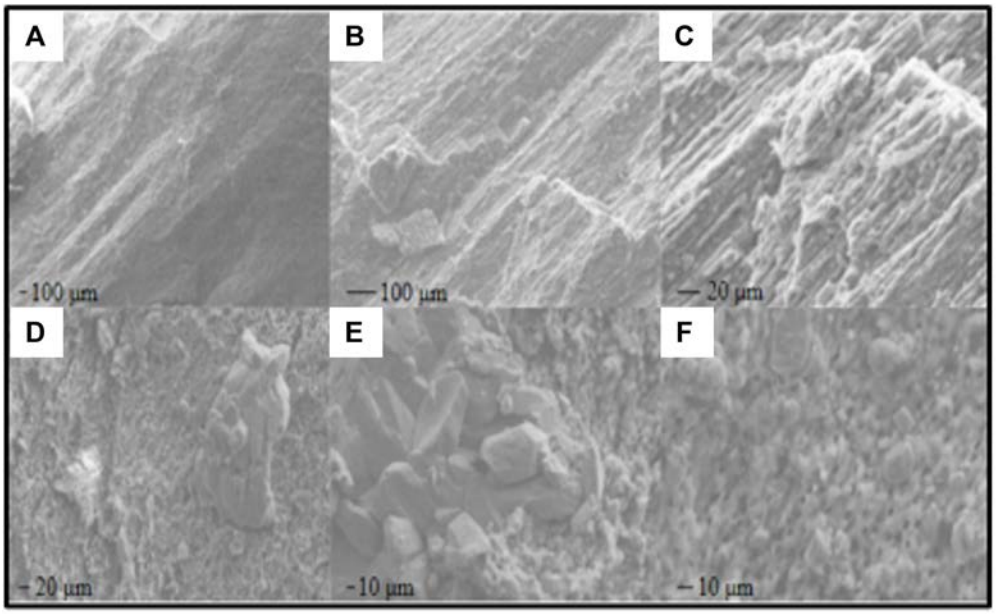

Figure 10. SEM images of specimen UISSM-001-COLA. (A through C) Tooth surface fragment. (D through F) Tuck surface fragment with scale.

er than those in the comparison to other proboscidean species, including *Mammuthus primigenius, Mammuthus primigenius fraasi, Mammuthus trogontherii, Mammuthus meridionalis,* and *Mammuthus columbi* (Table 2; Larramendi, 2015). Individuals of *M. columbi* exhibited ratios nearest in value to those of UISSM-001-COLA. The ratios found between the metacarpal (MTC) III length vs. radius length and manus height vs. radius length in UISSM-001-COLA were found to be smaller than those in the comparison to other proboscidean species, including *Mammuthus primigenius, Mammuthus primigenius fraasi, Mammuthus trogontherii, Mammuthus meridionalis,* and *Mammuthus columbi* (Table 3; Larramendi, 2015). Individuals of *M. columbi* exhibited ratios nearest in value to those of UISSM-001-COLA.

Specimen UISSM-001-COLA's right maxillary had high lamellar frequency and thick enamel; The specimen's tooth measurements match both those of *M. jeffersonii* and *M. columbi* specimens (Table 5). Although different molars were measured (M5 in the case of this study compared to M6 in the holotypes), consistent similarities between these two molars have been considered sufficient for taxonomic comparisons (Lister, 2017; Widga et al., 2017). After extracting and sequencing mtDNA from the molar, the results confirmed that UISSM-001-COLA belonged to haplogroup F (Enk et al., 2016), the lineage of North American mammoths that includes *M. columbi* and *M. jeffersonii* (Figure 13).

DISCUSSION

Pre- and Post-Mortem Analysis

Analysis of the percentage present and preservation quality (Table 1) of the bones indicate that some skeletal remains were fragmented and exposed to the surface. This is largely due to the absence of larger portions of the vertebral column and ribcage. There are rib bones missing and the ones that remain either have carnivorous gnaw marks or are in fragments. This leads us to conclude that the mammoth was exposed above the water before the remains were buried.

Interpretation of the enlarged pores in the autopodium bones suggest that they are evidence of premortem lesions or deformation caused by an underlying bone disease. The pathologies, specifically osteoporosis, surrounding manus and pes bones are found to be commonly associated with ulcers and weakening of

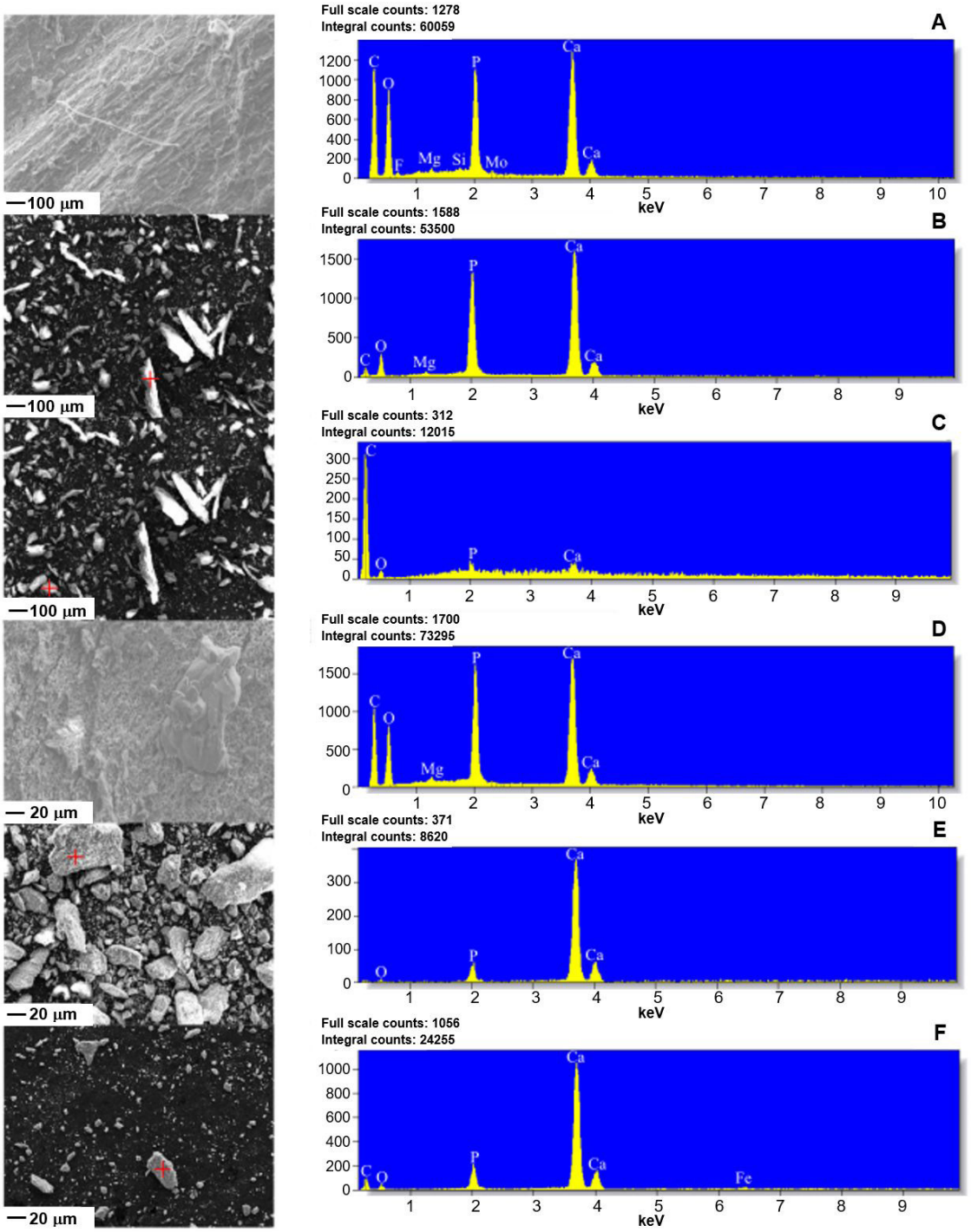

Figure 11. (A) SEM images of specimen UISSM-001-COLA tooth surface. (B through C) Interior tooth. (D) Tusk surface. (E through F) Interior bone with scale alongside respective energy dispersive X-ray spectroscopy (EDS) spectra. Red crosshairs represent the location of spot EDS analysis; images without crosshairs are alongside EDS spectra averaged across the full image.

the compact layer (Leshchinskiy, 2017). Pore widening within the vertebral column can be indicators of osteoporosis or other skeletal-related diseases such as Kashin-Beck disease (Krzeminska et al., 2015; Leshchinskiy, 2017). Defects within the spinous structure indicate the possibility of genetic defects or diseases (Krzeminska

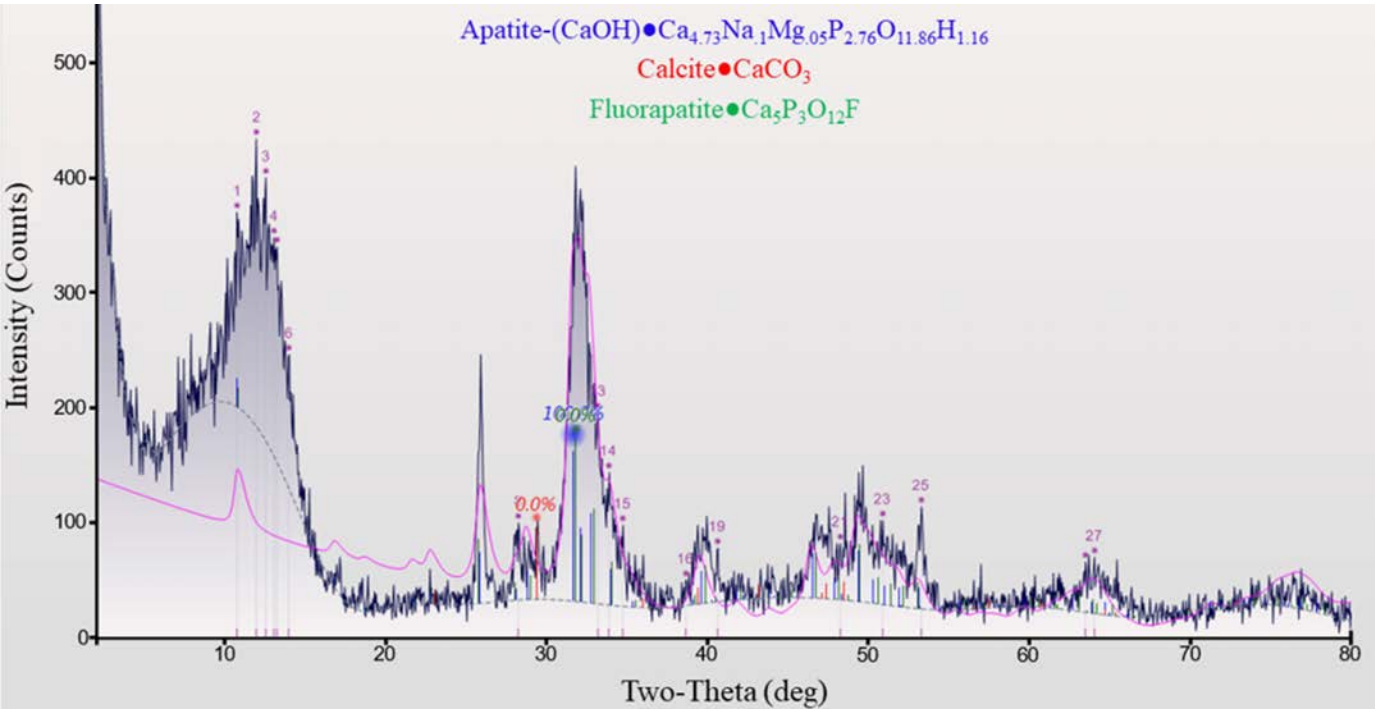

Figure 12. X-ray diffractogram of specimen UISSM-001-COLA tusk fragment. Analysis was performed at 40 kV. A total of 1561 data points were generated over a spectrum of 0 to 80°. Steps equaled 0.05° in measurements of two-theta.

et al., 2015). In addition, large marrow cavity openings into the vertebral foramen within the vertebrates of mammoths are also diagnostic of osteoporosis (Leshchinskiy, 2017).

The internal fracture in the calcaneum could be an indicator of lameness (Leshchinskiy, 2015; Leshchinskiy, 2017). There is also evidence that osteofibrosis-related conditions can cause increased bone fragility that may have led to this fracture (Krezerminska et al., 2015). These observations provide insights into possible bone diseases within the mammoth, whether it died because of bone disease or lameness, and pre- to postmortem states of the specimen. It is possible that the osteolytic conditions observed in UISSM-001-COLA could be representative of the broader implication that genomic defects may be correlated with the rise in osteolytic deformations within mammoths seen during the Late Pleistocene (Krezerminska et al., 2015; Leshchinskiy, 2015; Leshchinskiy, 2017; Rogers and Montgomery, 2017); however, further research on additional specimens would be required before this assertion can be made.

The study also provides an insight into the life of the mammoth's modern relative, the Asian elephant (*Elephas maximus*; Roca et al., 2015; Enk et al., 2016). Recent studies have shown a large trend in degenerative joint diseases within the Asian elephant populations (Luikart and Stover, 2005; Regnault et al., 2017). Studies into the endangered *E. maximus* also lead to the larger, ongoing question of a possible bottlenecking event among their ancient relatives. Studies suggest a low DNA diversity among both the modern Asian elephant and some species of mammoths including the *M. primigenius* (Vidya et al., 2005; Poinar et al., 2006; Vidya, 2016). Both *E. maximus* and mammoths have also faced similar population stressors such as habitat loss and over-predation (Saunders et al., 2010; Yansa and Adams, 2012; Gilmour et al., 2015; Vidya, 2016; Fisher, 2018).

Size, Age, and Gender Estimates

Podial to limb bone length ratios of UISSM-001-COLA (Table 2) suggest that the individual was smaller in body mass compared to the others within the Larrara-

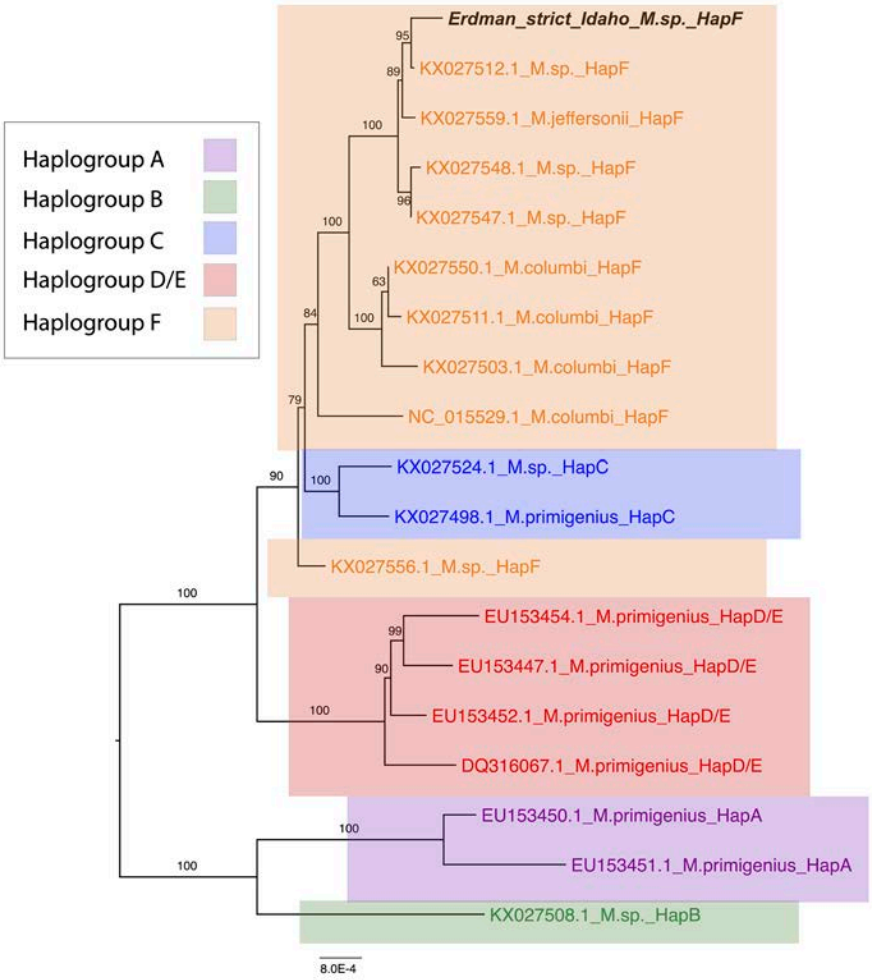

Figure 13. Maximum likelihood tree of speciemn UISSM-001-COLA's (Erdmand_strict_Idaho_M.sp_HapF) mtDNA from 100 RAxML bootstrap replicates. Specimen UISSM-001-COLA's mtDNA aligns strongly with Haplogroup F, which includes *M. columbi*, *M. jeffersonii*, and an unidentified mammoth.

mendi (2015) study. This may be due to the hypothesized age of the specimen at its time of death, corroborating that it was still a growing young adult. Specimen UISSM-001-COLA's height estimate at approximately 3.28 m (10.76 ft) places it out of the range of adult *M. primigenius* heights, which did not typically exceed 3 m (9.8 ft) but lies within the height range of adult *M. columbi,* whose maximum heights reached about 4 m (11–13 ft) at full maturity (Lister and Bahn, 2007). *M. jeffersonii* is largely a morphological descriptor for a form that might be a hybrid from introgression or a subspecies of *M. columbi.*

Gender differences exist in epiphyseal fusion rates, and it was pertinent to determine gender, even without a pelvis. If the mammoth were female, we would have observed many of its epiphysis fused to the diaphysis, or partially so, at the same time (Haynes, 2017). We observed many of the limb bones (proximal humerus, distal ulna and radius, and proximal femur) still unfused, which aligns with the fusing sequence of male mammoths, not females (Haynes, 2017; Figures 8 and 9). This epiphyseal fusion is consistent with the M5 designation (Figure 9). The proximal ulna and distal femur

were the key limb bones in intermediate stages of epiphyseal fusion to examine. Specimen UISSM-001-COLA died when the proximal ulna was fully fused, and the distal femur was almost completely fused.

Diagenetic Analysis

SEM/EDS, XRD, and protein analysis suggest that most of the protein and other organic components have degraded in the superficial areas of the tooth and tusk. Because the tusk has a more homogenous anatomy than the tooth and given that the tusk is, currently, highly and easily fragmented, little to no recoverable organic materials remain in the tusk. The degradation of proteins, lipids, and genetic materials in the bones likely mirrored that of the tusk. This is evidenced by the lack of protein found by preliminary protein analysis. Furthermore, a femur fragment tested for isotope analysis indicated that little to no collagen existed in the sample. Due to their molecular structures, proteins and lipids can generally be analyzed on longer temporal scales than genetic material (Briggs and Summons, 2014; Buckley and Wadsworth, 2014; Cappellini et al., 2018). Thus, because proteins are not detectable in the femur at the time of this writing, most, if not all of, the ancient organic biomolecules likely vanished from the bone.

The tooth, on the other hand, demonstrated more promising results of biomolecular preservation with the presence of high proportions of carbon in SEM/EDS analysis. The heterogeneity of elemental composition of the tooth may be explained by the protective barrier of enamel disrupting fossilization and degradation of the interior tooth (Trueman and Martill, 2002; Kendall et al., 2018). During the SEM/EDS analysis, it appeared that the smaller particles from the tooth tended to contain more carbon, perhaps due to differences in fragmentation of the denser enamel and the more porous, interior dentin. Additionally, it should be noted that likely surface contaminants may occur on the exterior of the tooth, which contained high levels of carbon according to EDS analysis. Whereas some level of contamination is inevitable, and the presence of these surface contaminants should be considered, it is unlikely that this contamination is significantly contributing to the elemental and molecular composition results.

The crystalline structures on the surface of the tusk may have arisen from one of two sources: first, these structures may be remnants of calcium carbonate from the depositional environment of UISSM-001-COLA or, second, they may represent a product of the process of efflorescence. Efflorescence occurs when carbon dioxide reacts with water to form carbonic acid, which then combines with calcium carbonate to form calcium bicarbonate. The calcium bicarbonate, a more soluble compound than calcium carbonate, can distribute and permeate into many areas of tusk. If the water begins to evaporate, the calcium bicarbonate is deposited on the exterior surface of the tusk as calcium carbonate. The process of efflorescence is evidenced by the finding of the crystalline structures on the surface of the tusk, but not on the other remains. This likely occurred to a greater extent in the tusk because of its porosity. The hard enamel on the surface of the tooth likely protected the teeth from calcite deposition. This finding is important to note, as the presence and absence of calcium carbonate crystals on the tusk and tooth, respectively, suggests that less water was able to seep into or evaporate off the tooth. Thus, the interior of the tooth is a good candidate for any future biomolecular analysis, as results further demonstrate that organic matter remains there.

Taxonomic Identification

Molars display different characteristics that are dependent on the tooth's state of wear and the age of the mammoth, which can cause challenges in species identification (Roth and Shoshani, 1988; Lister and Sher, 2015). With this said, the dimensions and characteristics of UISSM-001-COLA's right maxillary were compared to type specimens of *M. primigenius, M. columbi,* and *M. jeffersonii*. Although UISSM-001-COLA displays a high lamellar frequency (Table 5) similar for those reported for the type specimen of *M. jeffersonii* and neotype of *M. primigenius*, the plate number is still characteristic of *M. columbi*. Whereas these characteristics were used to make the taxonomic assignment, the amount of overlap between the measurements on UISSM-001-COLA and the values presented for each taxon causes uncertainty (Lister, 2017; Widga et al., 2017).

Haplogroup F is a clade of mammoths common to

the Great Plains and Great Basin, whereas haplogroup C is more common to the Yukon, Great Lakes, and East Coast. With that said, the differences between the mitochondrial genomes in these regions are minor and suggest that they all share a common matriline (Enk et al., 2016; Widga et al., 2017). Widga et al. (2017) suggest morphological overlap between populations of *Mammuthus* regionally and attribute this to varying environments and population history. Specimen UISSM-001-COLA's taxonomic placement is most closely related to the Great Plains and Great Basin mammoth group (haplogroup F).

It has also recently been proposed that mammoths occupying certain biogeographic ranges display variability between members of the same species (Widga et al., 2017). While most mammoth occurrences in Idaho have not been taxonomically described according to current morphometrics, Widga et al. (2017) observed biogeographic variation between mammoth occurrences in the western and eastern United States. Mammoths from the Great Plains, West Coast, and southwest have generally lower plate counts and thicker enamel than those from the Midwest and East Coast (Widga et al., 2017). A more detailed description of mammoth collections from Idaho, and by extension the northwestern U.S.A., is required to construct a more robust comparison of this variation.

CONCLUSION

Here, we determined that UISSM-001-COLA specimen was most likely a male mammoth 3.28 m (10.76 ft) tall at shoulder height, young adult around 29 years old (AEY), living 13,586 to 13,444 cal BP. Specimen UISSM-001-COLA was among some of the last mammoths to live on mainland of Western North America as mammoth populations became extremely endangered during the Bølling-Allerød climatic event. The mammoth died with potential lameness in one foot and potential bone disease and was preserved in an ancient terrestrial hot spring deposit. The cause of death is still undetermined. Over time, its remains underwent early stages of diagenetic alteration, and pores in the bones were infilled with recrystallized apatite and calcium carbonate. The incompleteness of the skeleton, along with the gnaw marks suggests partial disarticulation before ultimate burial. Still, many of the large bones were preserved in a low-energy environment.

While the driving forces of mammoth hybridization patterns are still not completely understood, they might represent interactions between distinct mammoth populations in response to the changing climate of the time. Whether this interbreeding was a direct result of climatic pressures remains unclear, but UISSM-001-COLA provides potential evidence of *M. primigenius* and *M. columbi* interaction. Extensive gene flow occurred between haplogroups C and F (Enk et al., 2016; Widga et al., 2017), and UISSM-001-COLA is designated into haplogroup F, the *M. jeffersonii* line. Specimen UISSM-001-COLA's death and subsequent preservation provides paleontologists with information about a key component to the ecosystem of Idaho. Further studies documenting other *M. jeffersonii* occurrences in Western North America will undoubtedly reveal more about the paleoecology and population dynamics of one of the Cenozoic's most eponymous taxa, as well as insights into underlying causes of their eventual extinction.

ACKNOWLEDGMENTS

This project was funded by the Office of Undergraduate Research Grant and the Hill Undergraduate Research Fellowship from Dr. Brian and Gayle Hill at the University of Idaho. The authors would like to acknowledge the help of Dr. Tom Williams at the University of Idaho for SEM/XRD expertise. Thank you to Dr. Lee Deobald at the University of Idaho Microchemistry Mass Spectrometry Laboratory and Gritman Medical Services in Moscow, Idaho, for donation of their CT scanner. Thank you to Shelby Dunn at UCSC Paleogenomics Lab for performing the DNA analysis on the mammoth specimen. Thank you to C. Widga from East Tennessee State University for his thoughtful conversations. Thank you to our reviewers for their insightful and helpful comments.

REFERENCES

Agenbroad, L.D., 2005, North American proboscideans—mammoths—the state of knowledge, 2003: Quaternary International, v. 126, p. 73–92.

Aguire, E. E., 1969, Revision sistematica de los Elephantidae por su morfología y morfometría dentaria. Estudios Geologicos, pt.s 2–3, no. 25 (123e177), p. 317–367.

Averianov, A.O., 1996, Sexual dimorphism in the mammoth skull, teeth, and long bones, *in* Shoshani, J., and Tassy, P., editors, The proboscidea—evolution and palaeoecology of elephants and their relatives: Oxford University Press, p. 260–269.

Barnosky, A.D., Lindsey, E.L., Villavicencio, N.A., Bostelmann, E., Hadly, E.A., Wanket, J., and Marshall, C.R., 2015, Variable impact of late-Quaternary megafaunal extinction in causing ecological state shifts in North and South America: Proceedings of The National Academy of Sciences, v. 113, no. 4, p. 856–861.

Biodiscovery, LLC dba Arbor Biosciences, 2018, myBaits—hybridization capture for targeted NGS Manual v4.01: Ann Arbor, Michigan, 17 p.

Björck, S., Berglund, B.E., and Digerfeldt, G., 1988, New aspects on the deglaciation chronology of South Sweden: Geographia Polonica, v. 55, p. 37-49.

Briggs, D.E., and Summons, R.E., 2014, Ancient biomolecules—their origins, fossilization, and role in revealing the history of life: BioEssays, v. 36, no. 5, p. 482–490.

Broecker, W.S., Andree, M., Wolfli, W., Osechger, H., Bonani, G., Kennett, J., and Peteet, D., 1988, The chronology of the last deglaciation—implications to the cause of the Younger Dryas Event: Paleooceanography, v. 3, no. 1, p. 1–19.

Buckley, M., and Wadsworth, C., 2014, Proteome degradation in ancient bone—diagenesis and phylogenetic potential: Palaeogeography, Palaeoclimatology, Palaeoecology, v. 416, p. 69–79.

Cappellini, E., Prohaska, A., Racimo, F., Welker, F., Pedersen, M.W., Allentoft, M.E., Damgaard, P.D.B., Gutenbrunner, P., Dunne, J., Hammann, S., Roffet-Salque, M., Ilardo, M., Moreno-Mayare, V.J., Wang, Y., Sikora, M., Vinner, L., Cox, J., Evershed, R.P., and Willerslev, E., 2018, Ancient biomolecules and evolutionary inference: Annual Review of Biochemistry, v. 87, p. 1029–1060.

Dabney, J., Knapp, M., Glocke, I., Gansauge, M.T., Weihmann, A., Nickel, B., Valdiosera, C., García, N., Pääbo, S., Arsuaga, J.L., and Meyer, M., 2013, Complete mitochondrial genome sequence of a Middle Pleistocene cave bear reconstructed from ultrashort DNA fragments: The Proceedings of the National Academy of Sciences, v. 110, no. 39, p. 15758–15763.

DeNiro, M.J., 1985, Postmortem preservation and alteration of in vivo bone collagen isotope ratios in relation to palaeodietary reconstruction: Nature, v. 317, p. 806–809, https://doi.org/10.1038/317806a0.

Doerner, J.P., and Carrara, P. E., 2001, Late Quaternary vegetation and climatic history of the Long Valley area, west-central Idaho, USA: Quaternary Research, v. 56, no. 1, p. 103-111.

El Adli, J.J., Cherney, M.D., Fisher, D.C., Harris, J.M., Farrell, A.B., and Cox, S.M., 2015, Last years and season of death of Columbian Mammoth from Rancho La Brea: Science Series, v. 42, p. 65–80.

Enk, J., Devault, A., Debruyne, R., King, C.E., Treangen, T., O'Rourke, D., Salzberg, S.L., Fisher, D., MacPhee, R., and Poinar, H., 2011, Complete Columbian mammoth mitogenome suggests interbreeding with woolly mammoths: Genome Biology, v. 12, p. 1–8.

Enk, J., Devault, A., Widga, C., Saunders, J., Szpak, P., Southon, J., Rouillard, J.-M., Shapiro, B., Golding, G. B., Zazula, G., Froese, D., Fischer, D. C. Macphee, R. D., and Poinar, H., 2016, *Mammuthus* population dynamics in late Pleistocene North America—divergence, phylogeography, and introgression: Frontiers in Ecology and Evolution, v. 4, no. 42, p. 1–13, https://doi.org/10.3389/fevo.2016.00042.

Fisher, D.C., 2009, Paleobiology and extinction of proboscideans in the Great Lakes region of North America *in* Haynes, G., editor, American megafaunal extinctions at the end of the Pleistocene: Vertebrate Paleobiology and Paleoanthropology, Springer, p. 55–75.

Fisher, D.C., 2018, Paleobiology of Pleistocene proboscideans: Annual Review of Earth and Planetary Sciences, v. 46, p. 229–260.

Gilmour, D.M., Butler, V.L., O'Connor, J.E., Davis, E.B., Culleton, B.J., Kennett, D.J., and Hodgins, G., 2015, Chronology and ecology of late Pleistocene megafauna in the northern Willamette Valley, Oregon: Quaternary Research, v. 83, no. 1, p. 127–136.

Graham, R., 1986, Taxonomy of North American mammoths, *in* Frison, G.C., and Todd, L.C., editors, The Colby Mammoth Site—taphonomy and archaeology of a Clovis Kill in Northern Wyoming: Albuquerque, University of New Mexico Press, 165–169.

Graham, R.W., and Lundelius, E.L., Jr., 2010, FAUNMAP II—new data for North America with a temporal extension for the Blancan, Irvingtonian and early Rancholabrean: FAUNMAP II Database, version 1.0 https://ucmp.berkeley.edu/faunmap/.

Haynes, G., 2017, Finding meaning in mammoth age profiles: Quaternary International, v. 443, p. 65–78.

Hedges, R.E.M., Millard, A.P., and Pike, A.W.G., 1995, Measurements and relationships of diagenetic alteration of bone from three archaeological sites: Journal of Archaeological Science, v. 22, p. 201–209.

Jans, M.M., 2008, Microbial bioerosion of bone—a review, *in* Wisshak, M., and Tapanila, L., editors, Current developments in dioerosion: Erlangen Earth Conference Series, Berlin, Heidelberg, Gernamy, Springer, https://doi.org/10.1007/978-3-540-77598-0_20.

Jones, R.W, and Bowers, A.W., 1968, Mammoth from Pleistocene spring deposits, Soda Springs, Idaho [abs.]: Northwest Sci-

ence, Northwest Scientific Association, v. 42–43, p. 35.

Keenan, S.W., Engel, A.S., Roy, A.L., and Bovenkamp-Langlois, G., 2015, Evaluating the consequences of diagenesis and fossilization on bioapatite lattice structure and composition: Chemical Geology, v. 413, p. 18–27.

Keenan, S.W., 2016, From bone to fossil—a review of the diagenesis of bioapatite: American Mineralogist, v. 101, no. 9, p. 1943–1951.

Kendall, C., Eriksen, A.M.H., Kontopoulos, I., Collins, M.J., and Turner-Walker, G., 2018, Diagenesis of archaeological bone and tooth: Palaeogeography, Palaeoclimatology, Palaeoecology, v. 491, p. 21–37.

Kirillova, I.V., Chernova, O.F., van der Made, J., Kukarskih, V.V., Shapiro, B., van der Plicht, J., Shidlovskiy, F.K., Heintzman, P.D., van Kolfschoten, T., and Zanina, O.G., 2017, Discovery of the skull of *Stephanorhinus kirchbergensis* (Jäger 1839) above the Arctic Circle: Quaternary Research, v. 88, no. 3, p. 537–550.

Krzeminska, A., and Wedzicha, S., 2015, Pathological changes of the ribs of woolly mammoths (*Mammuthus primigenius*): Quaternary International, v. 359–360, p. 186–194.

Krzeminska, A., Wojtal, P., and Oliva, M., 2015, Pathological changes on woolly mammoth (*Mammuthus primigenius*) bones—holes, hollows and other minor changes in the spinous processes of vertebrae: Quaternary International, v. 359-360, p. 178–185.

Larramendi, A., 2015, Proboscideans—shoulder height, body mass and shape: Acta Palaeontologica Polonica, v. 61, no. 3, p. 537–574.

Laws, R.M., 1966, Age criteria for the African elephant—*Loxodonta a. africana*: African Journal of Ecology, v. 4, no. 1, p. 1–37.

Lee, P.C., Sayialel, S., Lindsay, W. K., and Moss, C.J., 2012, African elephant age determination from teeth—validation from known individuals: African Journal of Ecology, v. 50, p. 9–20.

Leshchinskiy, S.V., 2012, Paleoecological investigation of mammoth remains from the Krakow Spadzista Street (B) site: Quaternary International, v. 276–277, p. 255–169.

Leshchinskiy, S.V., 2015, Enzootic diseases and extinction of mammoths as a reflection of deep geochemical changes in ecosystems of Northern Eurasia: Archaeological and Anthropological Sciences, v. 7, no. 3, p. 297–317.

Leshchinskiy, S.V., 2017, Strong evidence for dietary mineral imbalance as the cause of osteodystrophy in Late Glacial woolly mammoths at the Berelyokh site (Northern Yakutia, Russia): Quaternary International, v. 445, no. 25, p. 146–170.

Lewicki, J.L., Hilley, G.E., Dobeck, L., McLing, T.L., Kennedy, B.M., Bill, M., and Marino, B.D.V., 2013, Geologic CO_2 input into groundwater and the atmosphere, Soda Springs, ID, USA: Chemical Geology, v. 339, p. 61–70.

Lister, A.M., 1999, Epiphyseal fusion and postcranial age determination in the woolly mammoth *Mammuthus primigenius*: Deinsea, v. 6, no. 1, p. 79–88.

Lister, A.M., 2017, On the type material and evolution of North American Mammoths. Quaternary International, v. 443, pt. A, p. 14–31.

Lister, A.M., and Bahn, P., 2007, The natural history of mammoths, *in* Mammoths—giants of the Ice Age: London, UK, Frances Lincoln, p. 77–112.

Lister, A.M., and Sher, A.V., 2015, Evolution and dispersal of mammoths across the Northern Hemisphere: Science, v. 350, no. 6262, p. 805–809, https://doi.org/10.1111/j.1365-2028.1966.tb00878.x.

Luikart, K.A., and Stover, S.M., 2005, Chronic sole ulcerations associated with degenerative bone disease in two Asian elephants (*Elephas maximus*): Journal of Zoo and Wildlife Medicine, v. 36, no. 4, p. 684–688.

Maglio, V.J., 1973, Origin and evolution of the Elephantidae: Transactions of the American Philosophical Society, v. 63, no. 3, p. 1–149.

Malde, H.E., and Powers, H.A., 1962, Upper Cenozoic stratigraphy of western Snake River Plain, Idaho: Geological Society of America Bulletin, v. 73, no. 10, p. 1197–1220.

McCurry, M., Pearson, D.M., Welhan, J., Natwotniak, S.K., and Fisher, M., 2015, Origin and potential geothermal significance of China Hat and other late Pleistocene topaz rhyolite lava domes of the Blackfoot Volcanic Field, SE Idaho: Geothermal Resource Council, v. 39, p. 35–47.

Moss, C.J., 1996, Getting to know a population–studying elephants: Nairobi, African Wildlife Foundation, p. 58–74.

Ngure, N., 1996, What we can learn from tusks, *in* Kangwana, K., editor, Studying elephants: African Wildlife Foundation, Nairobi, Technical Handbook Series 7, p. 130–135.

Osborn, H.F., 1942, Proboscidea—a monograph of the discovery, evolution, migration and extinction of the mastodonts and elephants of the world, Stegodontoidea, Elephantoidea: New York, The American Museum Press, v. 2, p. 802.

Pilgrim, T., and Western, D., 1983, Tusk measurements provide insight into elephant population dynamics: African Elephant and Rhino Group Newsletter, v. 2, p. 16–17.

Pfretzschner, H.U., 2004, Fossilization of Haversian bone in aquatic environments: Comptes Rendus Palevol, v. 3, no. 6–7, p. 605–616.

Poinar, H.N., Schwarz, C., Qi, J., Shapiro, B., MacPhee, R.D., Buigues, B., Tikhonov, A., Huson, D.H., Tomsho, L.P., Auch, A., Rampp, M., Miller, W., and Schuster, S.C., 2006, Metagenomics to paleogenomics–large-scale sequencing of mam-

moth DNA: Science, v. 311, no. 5759, p. 392–394, DOI: 10.1126/science.1123360.

Regnault, S., Jonathon J.I., Dixon, Warren-Smith, C., Hutchinson, J.R., and Weller, R., 2017, Skeletal pathology and variable anatomy in elephant feet assessed using computed tomography: Peer J, v. 5, p. 2877.

Roca, A.L., Georgiadis, N., and O'Brien, S.J., 2005, Cytonuclear genomic dissociation in African elephant species: Nature Genetics, v. 37, no. 1, p. 96–100.

Roca, A.L., Ishida, Y., Brandt, A.L., Benjamin, N.R., Zhao, K., and Georgiadis, N.J., 2015, Elephant natural history—a genomic perspective: Annual Review of Animal Biosciences, v. 3, no. 1, p. 139–167.

Rogers, R.L., and Montgomery S., 2017, Excess of genomic defects in a woolly mammoth on Wrangel Island: Public Library of Science, Genetics, v. 13, no. 3, e1006601.

Roth, V.L., and Shoshani, J., 1988, Dental identification and age determination in *Elephas maximus*: Journal of Zoology, v. 214, no. 4, p. 567–588.

Saunders, J.J., Grimm, E.C., Widga, C.C., Campbell, G.D., Curry, B.B., Grimley, D.A., Hanson P.R., McCullum, J.P., Oliver, J.S., and Treworgy, J.D., 2010, Paradigms and proboscideans in the southern Great Lakes region, USA: Quaternary International, v. 217, no. 1–2, p. 175–187.

Sappington, R.L., 2019, Why are there no pre-Clovis mammoth sites in the Columbia Plateau?: Journal of Northwest Anthropology, v. 53, no. 2, p. 271–303.

Schmieder, R., and Edwards R., 2011, Quality control and preprocessing of metagenomic datasets: Bioinformatics, v. 27, no. 6, p. 863–864.

Stansfield, F.J., 2015, A novel objective method of estimating the age of mandibles from African elephants (*Loxodonta africana*): Public Library of Science One, v. 10, no. 5, e0124980.

Trueman, C.N., and Martill, D.M., 2002, The long-term survival of bone—the role of bioerosion: Archaeometry, v. 44, no. 3, p. 371–382.

Vereshchagin, N.K., and Tikhonov, A., 1986, A study on mammoth tusks: Proceedings of the Zoological Institute, USSR Academy of Sciences, v. 149, p. 3–14.

Vershinina, A.O., Kapp, J.D., Baryshnikov, G.F., and Shapiro, B., 2020, The case of an arctic wild ass highlights the utility of ancient DNA for validating problematic identifications in museum collections: Molecular Ecology Resource, v. 20, p. 1182–1190.

Vidya, T.N.C., 2016, Evolutionary history and population genetic structure of Asian elephants in India: Indian Journal of History of Science, v. 51, no. 2, p. 391–405.

Vidya, T.N.C., Fernando, P., Melnick, D.J., and Sukumar, R., 2005, Population differentiation within and among Asian elephant (*Elephas maximus*) populations in southern India: Heredity, v. 94, no. 1, p. 71–80.

Welhan, J.A., Gwyunn, M., Payne, S., McCurry, M., Plummer, M., and Wood, T., 2014, The Blackfoot volcanic field, southeast Idaho—a hidden high-temperature geothermal resource in the Idaho thrust belt, *in* Proceedings of the 39th Workshop on Geothermal Reservoir Engineering, February 24–26, 2014: Stanford, California, Stanford University, p. 1–13.

Welhan, J.A., and Breedlovestrout, R.A., 2016, Geothermal potential of the fold and thrust belt of southeast Idaho [abs.]: Geological Society of America Abstracts with Programs, v. 48, no. 6, doi: 10.1130/abs/2016RM-276023.

Widga, C., Saunders, J., and Enk, J., 2017, Reconciling phylogenetic and morphological trends in North American Mammuthus: Quaternary International, v. 443, p. 32–39.

Yacobi, Y., Shoshani, J., Hagos, Y., and Kebrom, E., 2004, The elephants (*Loxodonta africana*) of Zoba Gash Barka, Eritrea, part 3—Ecological and other data from tusks, teeth and carcasses: International Union for Conservation of Nature, v. 24, p. 44.

Yansa, C.H., and Adams, K.M., 2012, Mastodons and mammoths in the Great Lakes region, USA and Canada—new insights into their diets as they neared extinction: Geography Compass, v. 6, no. 4, p. 75–188.

Yushkevich, P., Piven J., Hazlett, H.C., Smith, R.G., Ho, S., Gee, J.C., and Gerig, G, 2006, User-guided 3D active contour segmentation of anatomical structures—significantly improved efficiency and reliability: Neuroimage, v. 31, no. 3, p. 1116–1128.

Supplemental Material

Inventory of the Bones

Spinose Process:

Catalog #	Scan ID (If Applicable)	Bone ID	% Intact	Measurements (length/width; cm)
SMS001	1-4	Vertebrae (Portion)	20	
SMS002	2-2	Lumbar Vertebrae	80	
SMS003	2-13	Vertebrae (Portion)	20	
SMS004	2-16	Sacrum	50	
SMS005	1-5	Atlas	100	
SMS006	2-12	Vertebrae (Portion)	10	
SMS007	1-16	Vertebrae (Portion)	40	
SMS008	2-17	Vertebrae (Portion)	50	
SMS009	1-2	Lumbar Vertebrae	60	
SMS010	1-8	Vertebrae (Portion)	20	
SMS011	1-18	Vertebrae (Portion)	60	
SMS012	1-11	Vertebrae (Portion)	40	
SMS013	1-10	Vertebrae (Portion)	5	
SMS014	2-1	Vertebrae (Portion)	15	
SMS015	1-20	Vertebrae (Portion)	10	
SMS016	1-19	Thoracic Vertebrae	70	
SMS017	2-3	Vertebrae	55	
SMS018	1-14	Thoracic Vertebrae	50	

Supplemental Material: Inventory of the Bones

Morrison, K., Usachenko N., Erdman, J., Waters, S., and Love, R.L.

Catalog #	Scan ID (If Applicable)	Bone ID	% Intact	Measurements (length/width; cm)
SMS019	1-12	Vertebrae (Portion)	25	
SMS020	1-15	Vertebrae (Portion)	10	
SMS021	1-7	Vertebrae (Portion)	5	
SMS022	2-6	Vertebrae	90	

Ribs:

Catalog #	Scan ID (if Applicable)	Bone ID	% Intact	Measurements (length/width; cm)
R001	9-21	Rib	N/A (so far)	26 / 7
R002		Rib	N/A (so far)	27 / 6
R003		Rib	N/A (so far)	10 / 4.5
R004	3-22	Rib	N/A (so far)	16 / 7
R005	3-11	Rib	N/A (so far)	14 / 9
R006		Rib	N/A (so far)	13 / 8
R007	3-1	Rib	N/A (so far)	16.5 / 7.5
R008		Rib	N/A (so far)	11.5 / 7
R009		Rib	N/A (so far)	21.5 / 5
R010		Rib	N/A (so far)	12 / 5
R011	3-25	Rib	N/A (so far)	15 / 6.5
R012	3-7	Rib	N/A (so far)	14.5 / 7.5
R013		Rib	N/A (so far)	10.5 / 4
R014	3-2	Rib	N/A (so far)	25.5 / 7
R015		Rib	N/A (so far)	22.5 / 6
R016	9-18	Rib	N/A (so far)	11.5 / 9
R017		Rib	N/A (so far)	10 / 5-7
R018		Rib	N/A (so far)	7.5 / 7.5
R019		Rib	N/A (so far)	12 / 6
R020		Rib	N/A (so far)	9 / 3.5
R021		Rib	N/A (so far)	7 / 4.5
R022		Rib	N/A (so far)	17 / 4.5
R023		Rib	N/A (so far)	13 / 5
R024		Rib	N/A (so far)	17 / 6
R025		Rib	N/A (so far)	11 / 6
R026		Rib	N/A (so far)	33 / 4

Supplemental Material: Inventory of the Bones

Morrison, K., Usachenko N., Erdman, J., Waters, S., and Love, R.L.

Catalog #	Scan ID (if Applicable)	Bone ID	% Intact	Measurements (length/width; cm)
R027		Rib	N/A (so far)	17 / 3.5
R028	9-12	Rib	N/A (so far)	27 / 3.5
R029		Rib	N/A (so far)	14 / 3.5
R030	9-6	Rib	N/A (so far)	33.5 / 4.5
R031	3-5	Rib	N/A (so far)	33 / 5
R032	9-16	Rib	N/A (so far)	31 / 5
R033		Rib	N/A (so far)	14.5 / 3.5
R034		Rib	N/A (so far)	11 / 3.5
R035		Rib	N/A (so far)	26 / 4.5
R036		Rib	N/A (so far)	36.5 / 5.5-4
R037		Rib	N/A (so far)	29.5 / 5
R038		Rib	N/A (so far)	27 / 5-4
R039		Rib	N/A (so far)	17.5 / 4
R040		Rib	N/A (so far)	9 / 4
R041	3-18	Rib	N/A (so far)	26 / 5-4.5
R042	3-16	Rib	N/A (so far)	28.5 / 5.5-4-3
R043	3-12	Rib	N/A (so far)	34 / 6-5
R044	9-14	Rib	N/A (so far)	13.5 / 5.5
R045		Rib	N/A (so far)	19 / 4.5
R046		Rib	N/A (so far)	9.5 / 5
R047		Rib	N/A (so far)	19.5 / 5.5-5
R048		Rib	N/A (so far)	10.5 / 4.5
R049		Rib	N/A (so far)	24.5 / 4.5-4
R050		Rib	N/A (so far)	14 / 5-4.5
R051		Rib	N/A (so far)	11 / 4.5
R052		Rib	N/A (so far)	11 / 5-4
R053		Rib	N/A (so far)	9 / 4.5
R054		Rib	N/A (so far)	46.5 / 3.5-3
R055		Rib	N/A (so far)	55.5 / 4-3.5
R056		Rib	N/A (so far)	16 / 7
R057		Rib	N/A (so far)	21.5 / 8
R058		Rib	N/A (so far)	23.5 / 4
R059		Rib	N/A (so far)	10 /3.5
R060		Rib	N/A (so far)	12 /3
R061		Rib	N/A (so far)	5 / 4.5
R062		Rib	N/A (so far)	9.5 / 3.5
R063		Rib	N/A (so far)	9 / 2.5
R064		Rib	N/A (so far)	6 / 2.5
R065		Rib	N/A (so far)	7 / 3

Supplemental Material: Inventory of the Bones

Morrison, K., Usachenko N., Erdman, J., Waters, S., and Love, R.L.

Catalog #	Scan ID (if Applicable)	Bone ID	% Intact	Measurements (length/width; cm)
R066		Rib	N/A (so far)	6 / 5
R067		Rib	N/A (so far)	9.5 / 4
R068		Rib	N/A (so far)	7 / 5
R069		Rib	N/A (so far)	9 / 3
R070		Rib	N/A (so far)	5.5 / 3
R071		Rib	N/A (so far)	16 / 3.5
R072		Rib	N/A (so far)	13 / 5-4
R073		Rib	N/A (so far)	13.5 / 3.5
R074		Rib	N/A (so far)	8 / 4
R075		Rib	N/A (so far)	6 / 3.5
R076		Rib	N/A (so far)	6.5 / 3.5
R077		Rib	N/A (so far)	11 / 3.5
R078		Rib	N/A (so far)	8 / 3.5
R079		Rib	N/A (so far)	11 / 3-2.5
R080		Rib	N/A (so far)	13 / 3
R081		Rib	N/A (so far)	8 / 2.5
R082		Rib	N/A (so far)	8 / 3
R083		Rib	N/A (so far)	4 / 3
R084		Rib	N/A (so far)	10 / 3.5
R085		Rib	N/A (so far)	7 / 2.5
R086		Rib	N/A (so far)	6.5 / 2.5
R087		Rib	N/A (so far)	7 / 4
R088		Rib	N/A (so far)	9 / 3
R089		Rib	N/A (so far)	11.5 / 3.5
R090		Rib	N/A (so far)	12 / 2.5
R091		Rib	N/A (so far)	8 / 4
R092		Rib	N/A (so far)	6 / 2.5
R093		Rib	N/A (so far)	6 / 3
R094		Rib	N/A (so far)	7 / 3
R095		Rib	N/A (so far)	9 / 3.5
R096		Rib	N/A (so far)	6 / 1.5
R097		Rib	N/A (so far)	4 / 3
R098		Rib	N/A (so far)	6.5 / 4
R099		Rib	N/A (so far)	15.5 / 4.5
R100		Rib	N/A (so far)	14 / 3.5
R101		Rib	N/A (so far)	12 / 3.5
R102		Rib	N/A (so far)	22.5 / 4
R103		Rib	N/A (so far)	8 / 5
R104		Rib	N/A (so far)	12 / 4

Supplemental Material: Inventory of the Bones

Morrison, K., Usachenko N., Erdman, J., Waters, S., and Love, R.L.

Catalog #	Scan ID (if Applicable)	Bone ID	% Intact	Measurements (length/width; cm)
R105		Rib	N/A (so far)	24 / 3.5
R106		Rib	N/A (so far)	14.5 / 3.5
R107		Rib	N/A (so far)	11 / 2
R108		Rib	N/A (so far)	9.5 / 3.5
R109		Rib	N/A (so far)	9.5 / 3
R110		Rib	N/A (so far)	8 / 2
R111		Rib	N/A (so far)	5.5 / 3
R112		Rib	N/A (so far)	6.5 / 4
R113		Rib	N/A (so far)	15.5 / 4
R114		Rib	N/A (so far)	7 / 4.5
R115		Rib	N/A (so far)	16.5 / 4.5
R116		Rib	N/A (so far)	10 / 4.5
R117		Rib	N/A (so far)	17 / 3.5
R118		Rib	N/A (so far)	9.5 / 4.5
R119		Rib	N/A (so far)	11 / 4
R120		Rib	N/A (so far)	10 / 3.5
R121		Rib	N/A (so far)	8 / 3
R122		Rib	N/A (so far)	9 / 4
R123		Rib	N/A (so far)	16.5 / 5.5
R124		Rib	N/A (so far)	6 / 3.5
R125		Rib	N/A (so far)	11.5 / 5
R126		Rib	N/A (so far)	6 / 3
R127		Rib	N/A (so far)	15.5 / 4
R128		Rib	N/A (so far)	7 / 2
R129		Rib	N/A (so far)	10.5 / 4
R130		Rib	N/A (so far)	5 / 3-2
R131		Rib	N/A (so far)	11 / 4
R132		Rib	N/A (so far)	6.5 / 2.5
R133		Rib	N/A (so far)	9 / 4.5
R134		Rib	N/A (so far)	4.5 / 3.5
R135		Rib	N/A (so far)	8 / 3.5
R136		Rib	N/A (so far)	6.5 / 3.5
R137		Rib	N/A (so far)	10 / 4
R138		Rib	N/A (so far)	10 / 3.5
R139		Rib	N/A (so far)	8.5 / 2.5
R140		Rib	N/A (so far)	12.5 / 3.5
R141		Rib	N/A (so far)	11.5 / 4
R142		Rib	N/A (so far)	13 / 3

Supplemental Material: Inventory of the Bones

Morrison, K., Usachenko N., Erdman, J., Waters, S., and Love, R.L.

Cranium:

Catalog #	Scan ID (If Applicable)	Bone ID	% Intact	Measurements (length/width; cm)
SMC001	11-36	Cranium (Portion)	15	
SMC002	11-45	Cranium (Portion)	15	
SMC003	11-46	Cranium (Portion)	15	
SMC004	11-4	Cranium (Portion)	15	
SMC005	11-30	Cranium (Portion)	95	
SMC006	11-24	Cranium (Portion)	95	
SMC007	11-15	Cranium (Portion)	15	
SMC008	11-16	Cranium (Portion)	5	
SMC009	11-17	Cranium (Portion)	5	
SMC010	11-18	Cranium (Portion)	2	
SMC011	11-19	Cranium (Portion)	20	
SMC012	11-21	Cranium (Portion)	10	
SMC013	11-27	Cranium (Portion)	15	
SMC014	11-41	Cranium (Portion)	5	
SMC015	11-43	Cranium (Portion)	10	
SMC016	11-44	Cranium (Portion)	10	
SMC017	11-38	Cranium (Portion)	10	
SMC018	11-40	Cranium (Portion)	10	
SMC019	11-8	Cranium (Portion)	2	
SMC020	11-6	Cranium (Portion)	10	
SMC021	11-42	Cranium (Portion)	10	

Catalog #	Scan ID (If Applicable)	Bone ID	% Intact	Measurements (length/width; cm)
SMC022	11-35	Cranium (Portion)	25	
SMC023	11-12	Cranium (Portion)	10	
SMC024	15-1	Lower Jaw/Mandible	80	76.2 / 50.8
SMC026	15-2	Right Tusk	90	228.6
SMC027	15-3 (possibly)	Left Tusk	90	
SMC028	15-1	Lower Left Molar (M1)	100	
SMC029	15-1	Lower Right Molar (M1)	100	
SMC030		Upper Left Molar	100	

Front Legs:

Catalog #	Scan ID (If Applicable)	Bone ID	% Intact	Measurements (length; cm)
SSMFL 1	7_1	Ulna	75	66.04
SSMFL 2	7_2	Humerus	90	38.10
SSMFL 3	7_3	Radius	85	63.50
SSMFL 4	7_4	Ulna	30	45.72
SSMFL 5	7_5	Ulna	30	59.63
SSMFL 6	7_6	Ulna	80	58.42
SSMFL 7	8_1	Humerus	90	90.17
SSMFL 8	8_2	Humerus	70	46.99
SSMFL 9	8_3	Radius	95	50.80

Catalog #	Scan ID (If Applicable)	Bone ID	% Intact	Measurements (length; cm)
SSMFL 10	8_4	Radius	45	19.05
SSMFL 11	8_5	Radius	50	22.86
SSMFL 12	8_6	Humerus	90	20.32
SSMFL 13	8_7	Radius	95	21.59
SSMFL 14	8_8	Radius	15	10.16
SSMFL 15	8_9	Radius	20	20.32

Rear Legs:

Catalog #	Scan ID (If Applicable)	Bone ID	% Intact	Measurements (length; cm)
SMRL001	4-1	Femur(distal)	40	51
SMRL002		Femur(distal)	50	73
SMRL003	4-5	Femur	15	45
SMRL004	4-6	Femur	15	41
SMRL005	4-7	Femur	15	44.5
SMRL006	5-1	Tibia	40	30.5
SMRL007		Tibia	20	33.7
SMRL008	5-2	Tibia3	40	37
SMRL009	5-6	Tibia 4	30	34
SMRL010	4-8	Patella 1	100	15.4
SMRL011	5-4	Pelvis 1	10	35.6
SMRL012	5-3	Pelvis 2	15	33.8

Supplemental Material: Inventory of the Bones

Morrison, K., Usachenko N., Erdman, J., Waters, S., and Love, R.L.

Catalog #	Scan ID (If Applicable)	Bone ID	% Intact	Measurements (length; cm)
SMRL013	6-6	Pelvis 3	10	29.6
SMRL014	6-4	Pelvis 4	10	28.7
SMRL015	5-5	Pelvis5	10	26.8
SMRL016	6-11	Pelvis 6	10	20.3
SMRL017	6-12	Pelvis 7	5	17.7
SMRL018	6-5	Pelvis 8	5	18
SMRL019	4-2	Pelvis 9	5	20.4
SMRL020	6-9	Pelvis 10	5	14.6
SMRL021	5-7	Pelvis 11	10	28.3
SMRL022	6-13	Pelvis 12	5	23
SMRL023	6-1	Pelvis 13	5	19.5
SMRL024	6-10	Pelvis 14	5	21
SMRL025	6-7	Pelvis 15	5	20.5

Supplemental Material: Inventory of the Bones

Morrison, K., Usachenko N., Erdman, J., Waters, S., and Love, R.L.

Forefeet:

Catalog #	Scan ID (If Applicable)	Bone ID	% Intact	Measurements length and width; cm)
SMF009		Cuneiform	80	10.5 / 9
SMF010		Magnum	50	8 / 10.5
SMF011		Unciform	96	15.5 / 10.5
SMF013		Trapezium	96	9 / 5
SMF014		Scaphoid	96	16 / 4
SMF016	14-8	Cuneiform	98	19 / 7
SMF017	14-7	Lunar	90	13.5 / 8
SMF018	14-11	Trapezium	98	9 / 4.5
SMF019	14-3	Pisiform	98	15 / 7
SMF020	14-4	Magnum	98	10.5 / 7.5
SMF021	14-6	Trapezoid	98	11 / 6

Hindfeet:

Catalog #	Scan ID (If Applicable)	Bone ID	% Intact	Measurements (length and width; cm)
SMF001		Calcaneum	98	24 / 19
SMF002		Calcaneum	97	24 / 18
SMF003		Astragalus	65	9 / 7
SMF004		Navicular	75	13 / 4.5
SMF005		External Cuneiform	98	10.5 / 6.5
SMF006		External Cuneiform	96	11 / 7
SMF007		Internal Cuneiform	98	8 / 5

Catalog #	Scan ID (If Applicable)	Bone ID	% Intact	Measurements (length and width; cm)
SMF008		Internal Cuneiform	96	7.5 / 5.5
SMF012		Astragalus	98	17.5 / 8
SMF015		Cuboid	98	14.5 / 5
SMF022		Navicular	50	11.5 / 5

Toes:

Catalog #	Scan ID	Bone ID	% Intact	Measurements (length and width; cm)
SMF023	14-9	Metacarpal	98	18.5 / 6.5
SMF024	14-1	Metacarpal	90	21 / 5.5
SMF025	14-2	Metacarpal	96	19 / 6
SMF026	10 -44	Metacarpal	90	20 / 6
SMF027		Metacarpal	96	19.5 / 7